In vivo modeling of human neuron dynamics and Down syndrome

Raquel Real[1,2#], Manuel Peter[3#], Antonio Trabalza[1#], Shabana Khan[1], Mark A. Smith[1], Joana Dopp[1], Samuel J. Barnes[4], Ayiba Momoh[3], Alessio Strano[3], Emanuela Volpi[5], Graham Knott[6], Frederick J. Livesey[3,7*] and Vincenzo De Paola[1*]

[1]Institute of Clinical Sciences, Faculty of Medicine, Imperial College London, UK, W12 0NN

[2]Graduate Program in Areas of Basic and Applied Biology, Instituto de Ciencias Biomedicas Abel Salazar, Universidade do Porto, 4050-313 Porto, Portugal

[3]Gurdon Institute and ARUK Stem Cell Research Centre, University of Cambridge, Tennis Court Rd, Cambridge, UK, CB2 1QN

[4]UK Dementia Research Institute, Division of Brain Sciences, Faculty of Medicine, Imperial College London, UK, W12 0NN

[5]University of Westminster, 115 New Cavendish Street London W1W 6UW, London

[6]EPFL, Lausanne, Switzerland, CH-1015

[7]UCL Great Ormond Street Institute of Child Health, 30 Guilford Street, London, WC1N 1EH

*Corresponding author. Email: vincenzo.depaola@imperial.ac.uk; r.livesey@ucl.ac.uk

[#]These authors contributed equally to this work.

Abstract

Harnessing the potential of human stem cells for modelling the physiology and diseases of cortical circuitry requires monitoring cellular dynamics *in vivo*. Here, we show that human iPSC-derived cortical neurons transplanted in the adult mouse cortex consistently organized in large (up to ~100 mm^3) vascularized neuron-glia territories with complex cytoarchitecture. Longitudinal imaging of >4000 grafted developing human neurons revealed that neuronal arbors refined via branch-specific retraction; human synaptic networks substantially restructured over 4 months, with balanced rates of synapse formation and elimination; oscillatory population activity mirrored the patterns of fetal neural networks. Finally, we found increased synaptic stability and reduced oscillations in transplants from two individuals with Down syndrome, demonstrating the potential of *in vivo* imaging in human tissue grafts for patient-specific modelling of cortical development, physiology and pathogenesis.

Cellular analyses in the human brain are restricted mainly to post-mortem material, which cannot provide direct observation of dynamic events such as anatomical refinement (*1*) and the emergence of complex patterns of network activity. This limitation raises the question of how to model human neuron dynamics and their dysfunction in the many incurable disorders that affect the developing cortex (*2*).

Rodent models have been valuable to the understanding of the pathophysiology of complex genetic disorders such as Down syndrome (*3-5*), which is associated with neurodevelopmental alterations and is caused by trisomy of chromosome 21 (Ts21), but certain phenotypes are better captured in the context of a human genetic background (*6*).

Human induced pluripotent stem cell (iPSC)-derived neurons can be used in patient-specific studies to model human cortical development (*7*), but *in vitro* 2D and 3D cultures (*8, 9*) lack key interactions with neuroglia and vasculature (*10*). There is an urgent need, therefore, to develop systems that more closely recapitulate the complex cellular dynamics of the living brain using patient-specific cells.

Building on previous transplantation work (*11*), we hypothesized that the existing physiological microenvironment in the adult mouse brain could support the expansion of human cortical tissue grafts from iPSC-derived neurons, thus allowing high-resolution, real-time *in vivo* monitoring of human neuron dynamics for extended periods of time.

Here, we used single-cell-resolution intravital microscopy (*12*) in human tissue grafts to gain insights into the dynamics of pruning, synaptogenesis and network activity during the earliest stages of cortical neuron development and demonstrated this approach by modelling human neuron structural and functional dynamics in Down syndrome.

Complex cytoarchitecture in human cortical tissue grafts

In order to study the dynamics of human axon and synaptic development and population activity *in vivo*, we generated cortical excitatory neurons from a control human iPSC line (*13*) (fig. S1) and transplanted them in the adult mouse somatosensory cortex (SCx1) for chronic multiphoton imaging (**fig. 1A**). Cells were transplanted after 36-38 days of differentiation, a stage at which cultures contained ~ 50% neural progenitor cells and ~ 50% deep layer cortical neurons (of which ~ 15% were T-box, Brain 1 (TBR1)+ and ~ 85% transcription factor interacting protein 2 (CTIP2)+, fig. S2A-B). As expected, and consistent with ongoing neurogenesis after engraftment, upper layer cortical excitatory neurons and a small proportion of astrocytes and oligodendrocytes could also be found both at 3 and 5 months post-transplantation (mpt) (fig. S2C-D). Electron microscopy confirmed that human grafts resembled immature cortical tissue at 130 days post-transplantation (dpt) (fig. S3A-C), with few synapses and few myelinated axons, and showed no detectable boundary with the mouse brain (fig. S3C), suggestive of structural integration (*14*). Importantly, the grafts contained proliferating cells (fig. S3C-D), enlarged in size (movie S1), and consisted of multiple human- and host-derived cell types (fig. S2, S3). The cell types from the host included microglial cells, oligodendrocytes, astrocytes and both excitatory neurons and inhibitory interneurons (fig. S3, D, E and F), while no interneurons of human origin were found (n = 3 transplants). Microglia recruitment in the graft was minimal (fig. S4). Post-mortem analysis revealed that the human tissue grafts developed organizational features

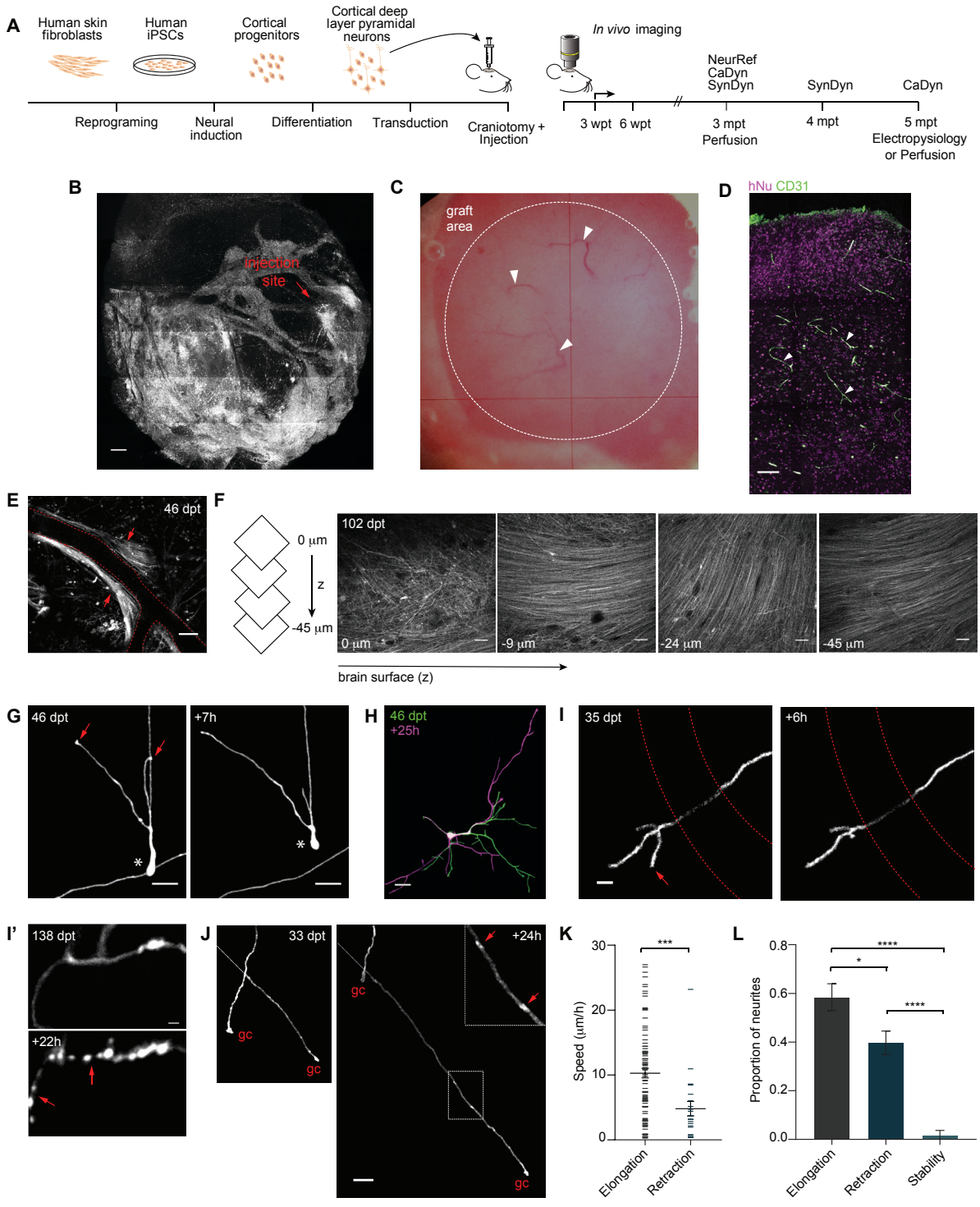

Figure 1. Single-cell-resolution *in vivo* imaging of human cortical tissue grafts reveals mechanisms of pruning. (**A**) Schematic of experimental design (left) and 2-photon *in vivo* imaging time line (right). NeuRef, neurite refinement. CaDyn, calcium dynamics. SynDyn,

synaptic dynamics. (**B**) Representative 2-photon overview of the cranial window over the injection site at 3 mpt. (**C**) Bright field view of a cranial window (~ 20 mm^2) at 5 mpt. Arrowheads indicate blood vessels. (**D**) Representative immunostaining of endothelial marker CD31 in the human graft at 5 mpt. Arrowheads indicate blood vessels. (**E**) Representative example of axonal bundles (arrows) along blood vessels; dashed red lines represent a blood vessel. (**F**) Representative example of axonal layering in human grafts. Same example as movie S3. (**G**) Example of a human neuron migrating (*) and remodeling the leading processes (arrows) over 7h. (**H**) Representative example of extensive remodeling of a dendritic arbor in a human pyramidal neuron over 25h. (**I**) Pruning of axonal branch over 6h. Dashed red lines represent a blood vessel. (**I'**) Neurite degeneration over 22h. Arrows indicate axonal fragments. (**J**) Representative examples of axon elongation and retraction over 24h. The arrows in the inset indicate EPBs. gc, growth cone. (**K**) Speed of neurite elongation and retraction at 3 mpt (n = 113 neurites from 104 cells in 6 animals, average 17 cells/animal). Mann-Whitney U-test, ***P < 0.001. (**L**) Proportion of neurites elongating, retracting and stable in 24h intervals at 3 mpt (n = 92 neurites from 88 cells in 6 animals, average 15 cells/animal). Bonferroni's multiple comparisons test after one-way ANOVA, $F_{2,15}$ = 43.74, P < 0.0001; *P < 0.05; ****P < 0.0001. Scale bars, 500 µm (B), 100 µm (D), 50 µm [(E) and (F)], 20 µm [(G), (H) and (J)], 10 µm (I), 2 µm (I').

resembling the structural arrangement of the early fetal cortex (fig. S5)(*15, 16*).

At earlier stages (< 2 mpt), cortical tissue grafts contained areas with ventricular zone-like territories, with cells positive for Paired box protein 6 (PAX6), a marker of neuronal progenitors, and Nestin, a marker for radial glia, which extended processes both radially outwards from the core of the rosette-like structures (fig. S5A), and arranged in parallel (fig. S5B), mimicking the organization of radial fibers in the intermediate zone of the human fetal cortex (*15*). Ki67-expressing proliferating cells were found in the inner apical layer, with doublecortin (DXC)-positive immature neurons towards its basal part, extending out into the rest of the graft (*16*) (fig. S5A). After 2 mpt, the rosettes did not persist and, although discrete cortical laminae were not clearly visible, consistent with the fact they form in late embryonic development (around 7-month post-conception) (*17*), immunostaining for deep and upper layer cortical neurons with antibodies for TBR1 and Special AT-rich sequence-binding protein 2 (SATB2), respectively, showed that these cell populations can segregate *in vivo* (fig. S5C). Human astrocytes were homogenously distributed in the cortical tissue grafts (fig. S5D). Finally, human tissue grafts were vascularized as shown *in vivo* and by the endothelial marker cluster of differentiation 31 (CD31) (**Fig. 1, B, C and D**), suggesting that the adult mouse brain microenvironment can support the development of a multicellular transplant.

Human axon pruning imaged *in vivo*

In order to track human neurons *in vivo*, we engineered them to express GFP via lentiviral-mediated transduction prior to transplantation. Human neurons were present for the duration of our experimental time-course, which spanned up to 6 months, and spread away from the injection site (**Fig. 1B**, on average up to 1.2 ± 0.6 mm (mean ± SD) from bregma in the

rostral direction over the first 3 mpt (*n* = 4 mice)). Consistent with the immature brain cell-cell interactions (*10*), human axons grew along blood vessels and as fiber bundles (**Fig. 1E,** movie S2), and parallel and radially oriented axonal layers could be detected below the dura mater (**Fig. 1F;** movie S3), similar to the ones found in human cortex (*18*).

Given the widespread axonal extension outside the graft area, we asked which brain regions human neurons target 5 mpt. Main SCx1 target areas showed a higher number of human fibers compared to areas known to receive fewer projections from SCx1 (fig. S6), suggesting the direction of axon elongation is targeted. For example, ipsilateral motor cortex, striatum, thalamus and contralateral SCx1 received more fibers than cerebellum and substantia nigra, and the corpus callosum had more axonal tracts compared to the internal capsule and cerebral peduncle, (fig. S6), as expected from rodent tracing experiments (*19*). These data provide evidence for long-range (over centimeters) axon growth of grafted human neurons through the mouse adult brain, and indicate that while human axons are either not responsive, or can overcome, the inhibitory signals present in the adult mouse brain, they may be directed by existing guidance cues or paths.

After an initial phase of growth (*20*), the selective pruning of axons and dendrites is thought to normally occur via retraction and degeneration during early development (*2, 21*). We explored the mechanisms of human neurite pruning up to 3 mpt (**Fig. 1G-L,** fig. S7A-B). At this stage, neurons were still migrating (**Fig. 1G**) and developing neural processes in a highly dynamic mode (**Fig. 1G-L**). We tracked the fate of 92 human neurites from 88 cells in 6 mice at 3 mpt (**fig. 1G-L**). While most neurites elongated in 24h (58.4 ± 5.5%), neurite refinement was dynamic, and interchanging retraction and elongation of individual neurites over 24 h (31.0 ± 2.1%) were observed (**Fig. 1I-L**). Developmental neurite degeneration

involves cytoskeletal destruction with widespread fragmentation over a time scale of 12-48 h (*22*), whereas retracting axons do not leave fluorescent fragments behind (*23*). Reducing the imaging interval from 24 h to 8 h showed that branch pruning (**Fig. 1I**) occurred mainly by retraction (91%), rather than degeneration (**Fig. 1I'**, 9%). Axonal *en passant* boutons (EPBs), one of the two types of presynaptic specialization on cortical axons (*24*), could be observed in branches with a growth cone elongating (**Fig. 1J)**. Neural processes extended long distances (maximum neurite extension = 462.769 µm in 24 h) at a speed of 10.29 ± 0.73 µm/h (**fig. 1K**), comparable to that observed in the neonatal mouse brain (*23*). Results were validated with tissue grafts from an independent control line (fig. S7A-B).

Human synaptic development imaged *in vivo*

Next, we studied the dynamics of synaptogenesis up to 4 mpt. Hallmarks of developing synaptic networks are 1) an increase in synaptic density over time, followed by pruning, and 2) the acquisition of a steady state with balanced rates of synaptic gain and loss (*25*). However, when and how human synaptic networks acquire these properties is unclear. We first considered dendritic spine formation and elimination (**Fig. 2A-F**).

After the initial phase of cell migration and neurite remodeling (**fig. 1G, H**), neurons stabilized allowing us to track the same cells over time (**fig. 2A**, fig. S8). Dendritic spines, the structural correlates of mammalian excitatory synapses (*26*), were seen as early as 20 dpt (32.8 ± 5.5 dpt, for either dendritic *filopodia*, considered the precursors of dendritic spines, or spines; *n* = 3 mice) (*27, 28*). We followed > 500 dendritic segments from 6 mice over days. However, for most dendrites, the density of synapses was too low to

quantitatively study the dynamics of dendritic spines before 3 mpt, as expected from previous human fetal cerebral cortex post-mortem work (*29*) and the early developmental stage modeled here. Eight neurons had sufficient dendritic spine numbers at 3 mpt to calculate spine density and turnover over 3-4 consecutive sessions of 48-hour intervals (up to 6 days). The average spine density was similar to human early fetal cerebral cortex (*29*) and constant over the imaging period (**Fig. 2C**, 0.043 ± 0.006 spines/μm; n = 70 spines present in the first session, 176 in total; Kruskal-Wallis test, $P > 0.05$). Synaptic structures were added and eliminated at equal rates even at these early developmental stages (**Fig. 2D**; Wilcoxon matched-pairs signed rank test, $P > 0.05$). The turnover ratio, a function of both spine gain and loss (*30*), was 46.9 ± 5.3% over 4 days (**Fig. 2E**), indicating synaptic reorganization.

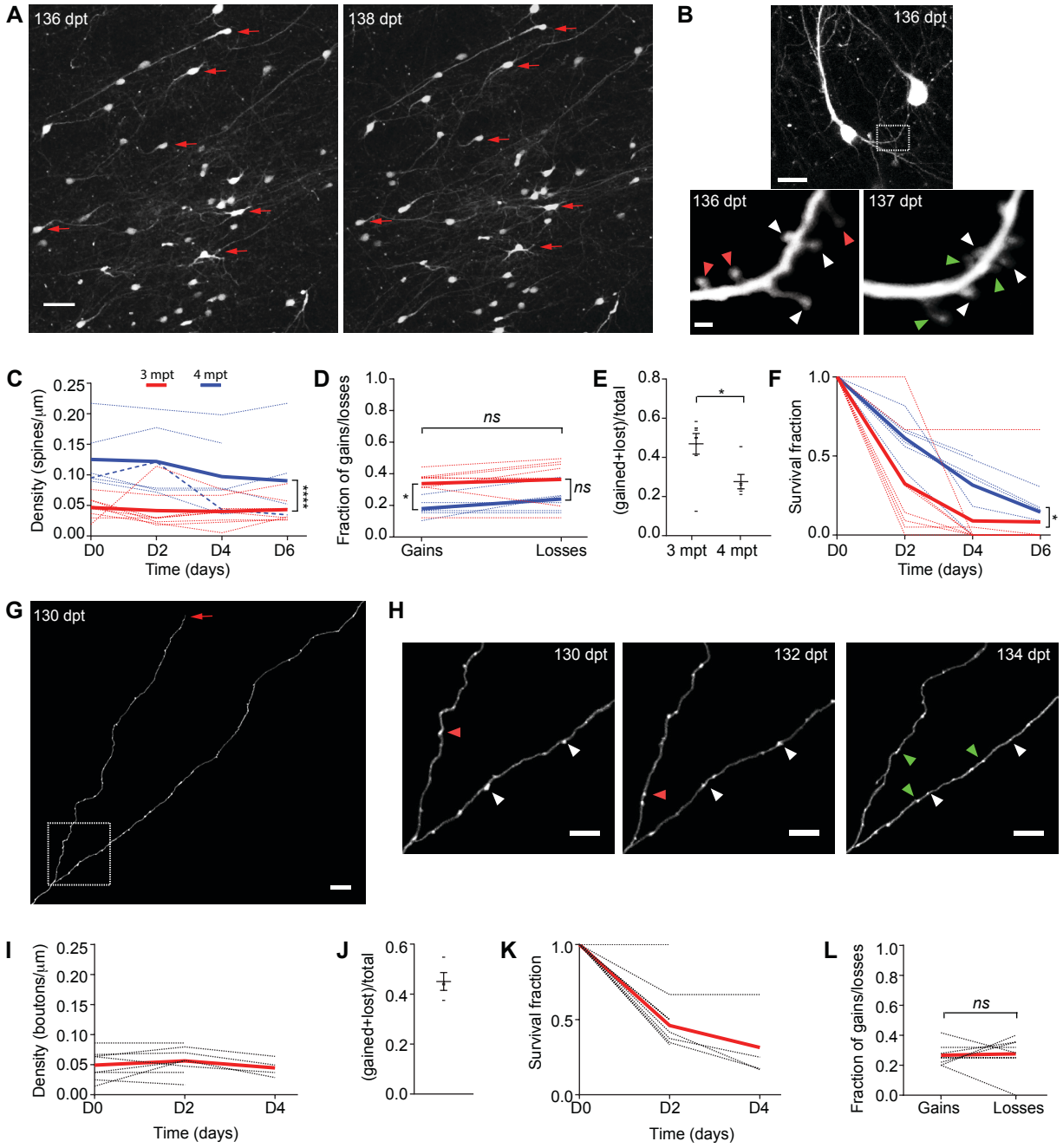

Figure 2. Developing human synaptic networks are characterized by substantial restructuring and balanced rates of gains and losses. (**A**) Overview of cranial window at 136 and 138 dpt; red arrows represent examples of cells with a stable location over a 48h period. (**B**) Detail of a representative dendrite imaged over 24h (white box in the top panel and red box in fig. S8A); green, red and white arrowheads indicate gained, lost and stable

dendritic spines, respectively. (**C**) Dendritic spine density over 4-6 days at 3 mpt (red: n = 8 cells, 1.40 mm total dendritic length, from 3 animals) and 4 mpt (blue: n = 6 cells, 0.93 mm total dendritic length, from 2 animals). Two-way ANOVA, interaction $F_{3,46}$ = 0.4357, P = 0.7285. ****P < 0.0001. (**D**) Average fraction of dendritic spines gained and lost over 48h at 3 mpt (red: n = 8 cells) and 4 mpt (blue: n = 6). Two-way ANOVA, interaction $F_{1,24}$ = 0.1894, P = 0.6673. Sidak's multiple comparisons test, *P < 0.05 (gains); P = 0.063 (losses). (**E**) Dendritic spine turnover rate (TOR) over 4 days at 3 mpt (n = 8) and 4 mpt (n = 6 cells). Mann-Whitney U-test, *P < 0.05. Each data point represents a cell. (**F**) Dendritic spines survival fraction at 3 mpt (red: n = 7 cells) and 4 mpt (blue: n = 6 cells). Two-way ANOVA, interaction $F_{3,47}$ = 1.513, P = 0.2235; *P < 0.05. (**G**) Representative example of a branched human axon at 130 dpt; arrow indicates a growth cone. (**H**) Detail of axon in (G), imaged every 48h over 4 days; green, magenta and white arrowheads indicate gained, lost and stable EPBs, respectively. (**I**) EPB density over 2-4 days at 3 mpt (n = 8 cells, 1.3 mm total axonal length, from 3 animals). One-way ANOVA, $F_{2,17}$ = 0.4014; P = 0.6756. (**J**) Quantification of EPB TOR over 4 days at 3 mpt (n = 4 cells). Each data point represents an axon. (**K**) Quantification of EPB survival fraction at 3 mpt (n = 8 cells). (**L**) Average fraction of EPB gains and losses over 48h at 3 mpt (n = 8 cells). Wilcoxon matched-pairs signed rank t-test; *ns*, not significant. Dashed lines represent individual cells and full lines represent means (C, D, F, I, K, L). Scale bars, 50 µm (A), 20 µm (B, top panel), 2 µm (B, bottom panel), 10 µm (G), 5 µm (H).

To investigate the development of synaptic remodeling over time we repeated the same experiment after one month. Again, spine density was constant over time (**Fig. 2C**, 0.112 ± 0.024 spines/μm; *n* = 171 spines present in the first session, 291 in total; Kruskal-Wallis test, $P > 0.05$). However, the average spine density was increased at 4 mpt. The majority of dendrites had balanced rates of dendritic spine gain and loss (**Fig. 2D**, paired two-tailed *t*-test, $P > 0.05$), and only in one cell we were able to capture net synaptic pruning over 2 days (**Fig. 2C**, thick dashed line), consistent with the idea that a major phase of synaptic pruning occurs only at later developmental stages (*28*).

The turnover ratio over 4 days was 27.6 ± 3.7%, which was lower than at 3 mpt (**Fig. 2E**). Consistently, the survival fraction, defined as the fraction of spines surviving as a function of time, was higher at 4 mpt (**Fig. 2F**), suggesting stabilization of dendritic spine dynamics over time.

To more thoroughly assess synaptic dynamics, we also studied presynaptic terminals along human cortical axons (**Fig. 2G-L**). The density of boutons remained stable over time (**Fig. 2I**, 0.051 ± 0.0075 EPBs/μm; *n* = 69 EPBs in the first session, 145 in total), indicating that axonal boutons were also added and eliminated at equal rates (**Fig. 2L**). The turnover rate over 4 days was 45.1 ± 3.6% (**Fig. 2J, K**), denoting comparable dynamics between dendritic spines and axonal boutons (at 3 mpt: Mann-Whitney *U*-test, $P = 0.3394$).

In summary, we were able to study early events of human cortical neuron synaptogenesis over the first 4 mpt. Despite the low synaptic density, consistent with the primordial stage modeled here (*29*), there are a number of conclusions we can draw on early *in vivo* human synaptic network development. First, transplanted human neurons initially formed synaptic structures within 4-12 weeks of *in vivo* development, similar to human fetal cerebral cortex

(*29*). Second, they underwent synaptic reorganization. Third, they progressively increased dendritic spine density over one month. Finally, human neurons balanced the rates of synaptic gain and loss over a time scale of few days.

Functional human cortical networks imaged *in vivo*

Patterned neural activity is thought to be fundamental to neural circuit development in the immature brain (*31, 32*). While spontaneous and sparse activity can be detected in human cortical network preparations *in vitro*, recapitulating patterns typical of early human cortical population activity, such as recurrent oscillatory bursts (*32*), remains challenging (*33, 34*).

We first investigated the electrophysiological properties of transplanted cells. We performed *ex vivo* whole-cell recordings in coronal brain slices containing the grafts (fig. S9). Current-clamp recordings were made from 18 pyramidal shaped somas (*n* = 4 mice), as identified by differential interference contrast microscopy, expression of either GFP or Td-Tomato, and by filling neurons with Lucifer yellow dye prior to post-hoc anatomical inspection (fig. S9A). Patched grafted pyramidal-like neurons were at different stages of biophysical maturation and development, with an average resting membrane potential of -53.8 ± 1.7 mV, average capacitance of 19.4 ± 2.2 pF and average input resistance of 1.4 ± 0.1 GΩ. While cells were quiescent at resting membrane potentials, depolarizing current-steps evoked action potential firing in all pyramidal neurons tested (fig. S9B), with average action potential amplitudes of 91.3 ± 2.6 mV and half-widths of 2.2 ± 0.2 ms.

Immunohistochemistry showed glutamatergic and GABAergic terminals within the human graft (Fig. S10 A and B). To confirm that human neurons received both excitatory and inhibitory input, pyramidal shaped neurons were voltage-clamped (-70 mV) and spontaneous miniature excitatory synaptic currents (mEPSC) were observed at a frequency of 0.30 ± 0.05 Hz (5 out of 18 neurons) with an amplitude of 20.1 ± 3.2 pA, which was completely blocked by the α-amino-3-hydroxy-5-methyl-4-isoxazolepropionic acid (AMPA) receptor antagonist 2,3-dihydroxy-6-nitro-7-sulfamoyl-benzo-quinoxaline-2,3-dione (NBQX) (*n* = 4). Although synaptic events were observed in the remaining neurons, spontaneous frequency was insufficient to acquire enough events for statistical analysis (fig. S9C and S7C-D). Using a high chloride (130 mM) internal solution and in the presence of NBQX, spontaneous miniature inhibitory synaptic currents (mIPSC) were observed at a frequency of 0.24 ± 0.12 Hz (3 out of 6 neurons) with an amplitude of -73.3 ± 21.0 pA, that was fully inhibited by bicuculline (*n* = 3) (fig. S9C). Similar to mEPSC, inhibitory synaptic events were observed in the remaining neurons but insufficient events were acquired for detailed kinetic analysis. In summary, grafted neurons are excitable and fire action potentials. In addition, they receive both excitatory and inhibitory input, suggesting functional network connectivity.

To determine the origin of the afferent synaptic input to the functionally active neurons, we performed monosynaptic retrograde tracing using a modified rabies virus. This virus lacks a glycoprotein needed for replication and can only infect cells expressing the avian tumor virus receptor A (TVA) (fig. S11). Human iPSC-derived cortical progenitors and neurons were transduced with a lentiviral vector containing the TVA, nuclear GFP and glycoprotein, under the control of the human synapsin promoter (fig. S11A). Five months

after the transplantation, the modified mCherry expressing-rabies virus was injected in the same location, where only grafted cells expressing the TVA are susceptible to infection. Cells that are monosynaptically connected to the infected human cells also become infected and express mCherry, allowing for accurate tracing of the neural input to the cells in the human grafts (fig. S11B). We observed that while most of the input to the transplanted human neurons comes from other human neurons (92.5% ± 1.5%, *n* = 4333 cells in 2 brains), host neurons also innervate the human graft (7.5% ± 1.5%, *n* = 397 cells in 2 brains) (fig. S11C). The traced host neurons were located within the graft, in the cortical areas adjacent to the graft, in the contralateral cortex, and in the ipsilateral CA1 hippocampal region (fig. S11B). While no traced neurons were found in other subcortical regions, thalamocortical terminals were present in the graft (fig. S10; see also fig. S12) (*20*). These results provide evidence that most synaptic input to the grafts comes from other human neurons. Furthermore, since no interneurons of human origin were found, these data, together with the demonstration that human neurons in the graft receive inhibitory input (fig. S9C, bottom panel), suggest that inhibition in the human grafts comes from the host.

To assess the functional development of cortical networks *in vivo*, we engineered neurons to express the genetically encoded calcium indicator GCaMP6s (*35*) prior to grafting and studied calcium-mediated neuronal activity *in vivo* (**Fig. 3**; *n* = 8 mice). Spontaneous, sparse activity (**Fig. 3A-C**) was detected as early as 2 weeks post-transplantation (wpt) and persisted up to 3 mpt (**Fig. 3C**). In addition, bursts of activity synchronized across the neuropil and multiple cells (*31*) were also detected at 1 mpt (**Fig. 3C,** inset) and persisted in all grafts tested up to 5 mpt (fig. S7E-H and movies S4, S5).

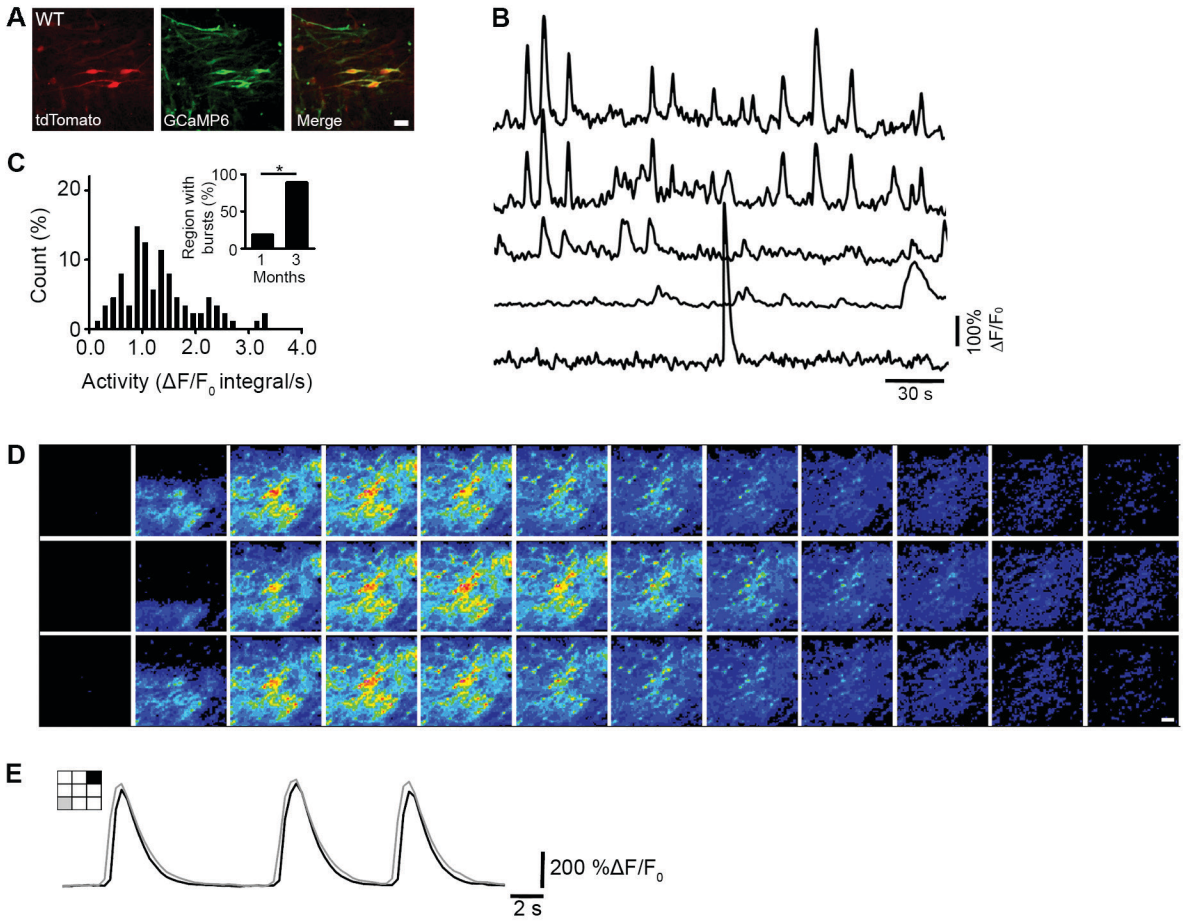

Figure 3. *In vivo* calcium imaging shows that patterned population activity emerges early and has a defined spatiotemporal order. (**A**) Example of an imaged cortical region taken from a WT-1 graft at 1 mpt in the somatosensory cortex of an adult mouse. Neurons express tdTomato (left - red) and GCaMP6 (middle - green). GCaMP positive neurons are shown as a maximum intensity projection of activity over a 4 min period of spontaneous activity. Active neurons (yellow) are shown by overlaying the images (right – merge). (**B**) Representative $\Delta F/F_0$ calcium traces from 5 active neurons imaged in a WT-1 graft at 1 mpt. (**C**) Distribution of spontaneous calcium activity in WT-1 grafts at 1-2 mpt. Activity was measured as the integral of the average $\Delta F/F_0$ signal over the entire region of interest (ROI), normalized to the total duration of the recording in seconds (*n* = 88 cells, 6 ROIs, 3 mice).

Inset: percentage of ROIs in WT-1 grafts at 1-2 mpt (3 out of 16 ROIs, 18.8%; *n* = 4 mice) and 3 mpt (31 out of 35 ROIs, 89.0%; *n* = 5 mice) that exhibit bursts. Chi-square test, **P* < 0.05. (**D**) Montage of image frames from a typical recurrent burst in a WT-1 graft. (**E**) Example of burst activity over two different spatial regions (gray and black) shown in left cartoon, taken from the bursts in (D). Scale bars, 10 μm (A), 20 μm (D).

Many of these bursts had a defined spatiotemporal order (**Fig. 3D,E**), as well as recurrent oscillatory behavior (< 1 Hz between events; **fig. 3D** and S7E-I), with different incidence between 1 and 3 mpt (**Fig. 3C,** inset), resembling activity recorded in human developing cortex (*36, 37*), and consistent with a report on transplanted human cerebral organoids (*38*).

Recordings of calcium signals with air-puff stimulation of the animal's whiskers and facial skin, revealed that grafted neurons in the primary somatosensory cortex can be responsive to sensory stimulation (fig. S12; ~ 30% of the stimulation trials in one mouse; neither of the other two animals tested showed sensory-evoked activity), indicating that thalamocortical synapses can functionally drive activity in the human graft at 6 mpt.

Imaging human neuron structural and functional dynamics in Down syndrome

So far, we have characterized the structural and functional dynamics of human cortical neurons during the earliest phases of their development *in vivo* (**fig. 1-3**) and validated the main results with neurons from an independent control iPSC-line (WT-2, fig. S7). To model the *in vivo* dynamics of pruning, synaptogenesis and network activity in a complex genetic disorder, we first generated iPSC-derived progenitors and neurons from two individuals with Down syndrome (fig. S1), and then transplanted them in adult immunodeficient mice. During the reprogramming process of one of these lines (Ts21-2), we identified a disomic clone that had lost one extra copy of human chromosome 21 (Hsa21) (WT-2) (*39-41*). We used a microsatellite short tandem repeat (STR) assay to confirm that the parental fibroblast population was not mosaic for disomy and trisomy 21, and that Ts21-2 and WT-2 are otherwise identical to each other and the initial fibroblasts (fig. S13). This revertant disomic line (WT-2) allowed us to highlight phenotypes caused by an extra copy of Hsa21, rather than by genetic differences between individuals, without the need for multiple control lines, typically required to control for genetic variations or diverse differentiation potencies observed in genetically distinct human iPSC lines (*42*). Genome-wide copy number single nucleotide polymorphism (SNP) assay confirmed that the two Ts21 iPSC lines had normal karyotype, except for the extra copy of Hsa21 (fig. S14). Fluorescence In Situ Hybridization (FISH) on cortical tissue grafts further verified the presence of the extra copy of Hsa21 (fig. S15). The Ts21 lines generated progenitors, neurons and proliferating cells similarly to control grafts at 5 mpt (fig. S16 and fig. S17). Astroglia, however, were overproduced in Ts21 grafts (fig. S16), recapitulating the human pathology (*43*). Ts21 neurons were also

present in stable locations to the end of our experimental timeline, allowing for *in vivo* single-cell-tracking (fig. S18). Chronic *in vivo* imaging revealed that Ts21 neurons had similar rates of axon growth/retraction compared to control neurons at 3 wpt (**fig. 4A-D**), suggesting normal early developmental axon refinement. In addition, Ts21 neurons in the graft formed morphologically mature synaptic structures, which were plastic over time (**fig. 4E-L**). To determine whether dendritic spine growth was associated with synapse formation in Ts21 neurons, we reconstructed in one transplant, with electron microscopy (EM), a subset of the same dendrites after long-term *in vivo* imaging (**fig. 4E, F, G**). We found that newly formed dendritic spines formed synapses in 14 out of 34 cases (41%) and 6 of them (6 out of 14, 43%) within 48 hours of their first appearance. Serial EM reconstructions revealed that human dendritic spines and presynaptic terminals contained a postsynaptic density and synaptic vesicles, respectively, suggestive of complete synaptic maturation (**fig. 4G**). Indeed, whole-cell recordings from coronal brain slices containing the Ts21 grafts showed normal synaptic input on the DS-donor derived neurons compared to control (fig. S19, A to D), suggesting functional synaptic connections. Longitudinal *in vivo* imaging, however, showed that dendritic spines, and to a lesser extent synaptic boutons (**fig. 4J-L)**, were more stable in neurons from both individuals with DS than in control, as demonstrated by higher survival and reduced turnover (**fig. 4H, I;** fig. S20). High density of GFP positive neurons prevented a quantitative analysis of synaptic dynamics in the WT-2 line. To understand whether the higher dendritic spine survival rates in Ts21 lead to higher spine density, we quantified dendritic spine density across the four lines. We found an increase in dendritic spine density in neurons from the Ts21-1 compared to WT-1 (fig. S21A), althought this increase did not reach significance consistent with post-mortem fetal DS brain analysis at ~

5-8 gestational months (*27*). However, we found higher spine densities in Ts21-2 compared to WT-2, our most reliable comparison (fig. S21A). Putting the data from the two Ts21 and WT lines together highlighted a significant spine density increase in the Ts21 cells (fig. S21B). Overall, these data raise the possibility that spine density in DS cortical neurons could be higher than control, at least at the early developmental stages tested here. No difference in EPB density was found across the four lines (fig. S21 C and D).

To investigate further the increased synaptic stability phenotype, we studied neural population activity, a main regulator of postnatal synaptic refinement and stabilization (*26*), through *in vivo* calcium imaging of GCaMP6-expressing Ts21 grafts (**fig. 4M-N**). We measured both burst and global activity (see methods). These measures were reduced in Ts21 grafts (**fig. 4O-Q**). Together, these data highlight *in vivo* synaptic stability and functional early cortical network phenotypes in DS.

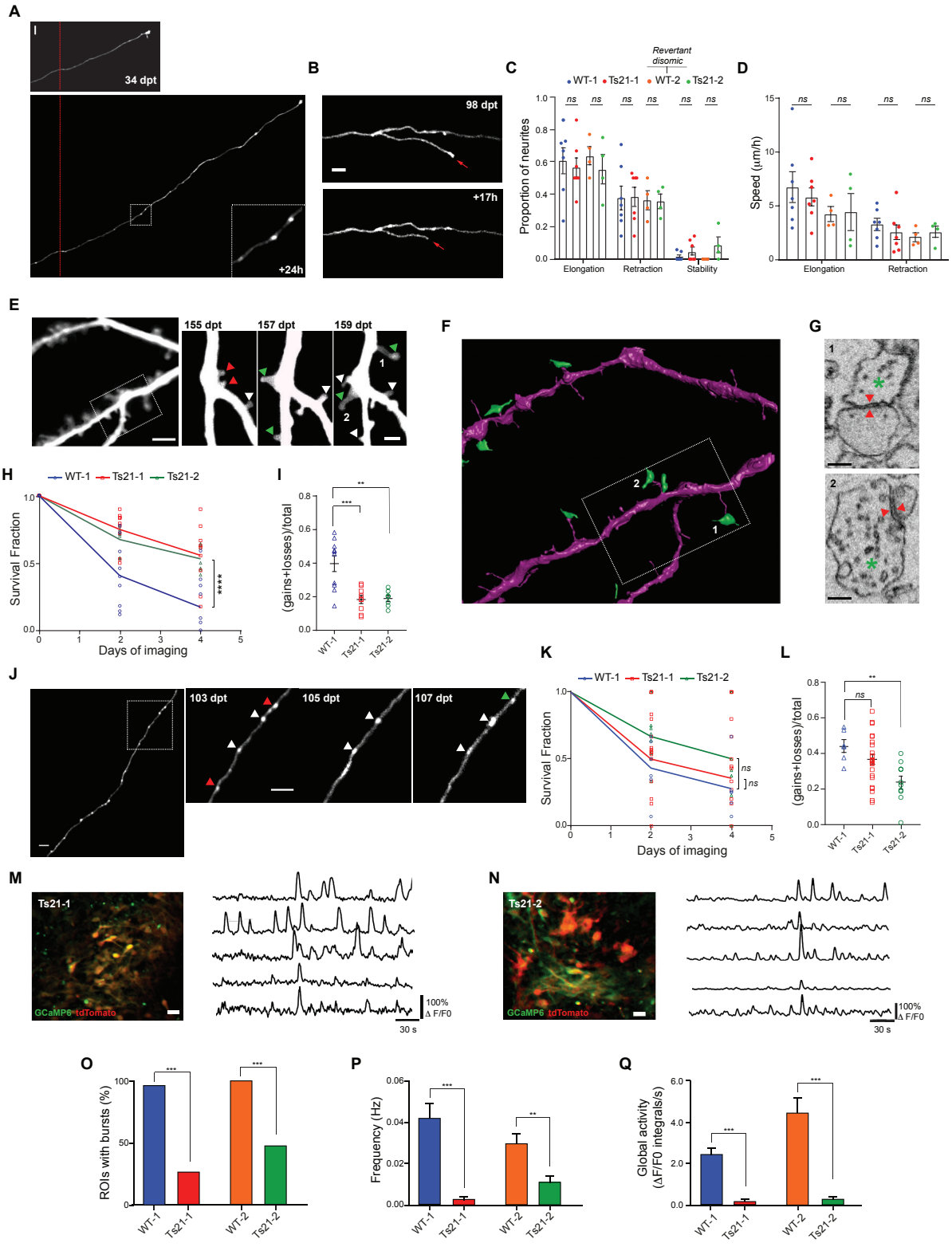

Figure 4. *In vivo* modelling of structural and functional neuronal dynamics in tissue

grafts from individuals with Down syndrome. (**A**) Representative example of axon elongation in a Ts21-1 neuron, over a 24h period. The inset highlights the presence of EPBs. (**B**) Example of axonal branch retraction in a Ts21-1 neuron over 17h. (**C**) Proportion of elongating, retracting and stable neurites in 24h intervals in WT-1 (*n* = 96 neurites from 79 cells, 7 grafted animals, average 11 cells/animal), Ts21-1 (*n* = 65 neurites from 60 cells, 7 grafted animals, average 9 cells/animal), WT-2 (*n* = 65 neurites from 53 cells, 4 grafted animals, average 13 cells/animal) and Ts21-2 (*n* = 60 neurites from 51 cells, 4 grafted animals, average 13 cells/animal) grafts at 3 wpt. WT-2 is a revertant disomic cell line from Ts21-2. Unpaired two-tailed *t*-test; *ns*, not significant. Each data point represents an animal. (**D**) Speed of neurite elongation and retraction in WT-1 (*n* = 96 neurites from 73 cells, average 10 cells/animal), Ts21-1 (*n* = 62 neurites from 54 cells, average 8 cells/animal), WT-2 (*n* = 53 neurites from 47 cells, average 12 cells/animal) and Ts21-2 (*n* = 54 neurites from 46 cells, average 12 cells/animal) grafts at 3 wpt. Unpaired multiple *t*-test; *ns*, not significant. Each data point represents an animal. (**E**) Example of dendritic branches and spines on a Ts21-1 neuron, imaged at 48h intervals for 4 days; green, red and white arrowheads indicate gained, lost and stable dendritic spines, respectively. (**F**) 3D-rendering of the same dendritic region imaged *in vivo* in (E), obtained from electron microscopy reconstruction. Presynaptic terminals are shown in green. (**G**) Electron microscopic images of the dendritic spines marked with 1 and 2 in (E). Red arrows indicate the location of synapses. Green asterisk, presynaptic terminal. (**H**) Dendritic spines survival fraction over 4 days in WT-1 (*n* = 10 cells from 2 animals), Ts21-1 (*n* = 9 cells from 4 animals) and Ts21-2 (*n* = 7 cells from 2 animals) grafts at 3-4 mpt. Two-way ANOVA, interaction $F_{4,69} = 5.435$, $P = 0.0007$; Tukey's multiple comparisons test, ****$P < 0.0001$. Each data point represents

a cell. (**I**) Quantification of dendritic spine turnover rate over 4 days in WT-1 (*n* = 10 cells from 2 animals), Ts21-1 (*n* = 9 cells from 4 animals) and Ts21-2 (*n* = 7 cells from 2 animals) grafts at 3-4 mpt. Sidak's multiple comparisons test after one-way ANOVA, $F_{2,23}$ = 3.078, ***P* < 0.01; ****P* <0.001. Each data point represents a cell. (**J**) Representative example of an axon on a Ts21-2 neuron imaged at 48h intervals for 4 days. The arrowheads in the insets indicate stable (white), new (green) and lost EPBs (red). (**K**) EPBs survival fraction over 4 days in WT-1 (*n* = 6 cells), TS21-1 (*n* = 24 cells) and TS21-2 (*n* = 10 cells) grafts at 3-4 mpt from 3 mice each. Two-way ANOVA, interaction $F_{4,111}$ = 0.8211, *P* = 0.5144; *ns*, not significant. Each data point represents an axon. (**L**) EPBs turnover rate over 4 days in WT-1 (*n* = 6 cells), TS21-1 (*n* = 24 cells) and TS21-2 (*n* = 10 cells) grafts at 3-4 mpt from 3 mice each. Sidak's multiple comparison test after one-way ANOVA, $F_{2,37}$ = 5.588, ***P* < 0.01; *ns*, not significant. Each data point represents an axon. (**M**)**,** (**N**) Left: Example of imaged cortical regions taken from Ts21-1 (M) and Ts21-2 (N) grafts in the somatosensory cortex of adult mice. Neurons express tdTomato (red) and GCaMP6s (green). Active neurons (yellow) are shown by overlaying the images. Right: Representative $\Delta F/F_0$ calcium traces from 5 active neurons imaged in Ts21-1 (M) and Ts21-2 (N) grafts. Note weak synchronized burst activity across different neurons compared to the traces in fig. S7E. (**O**) Percentage of ROIs in WT-1 (50 out of 52 ROIs, 96.1 %, 6 grafted mice), Ts21-1 (10 out of 38 ROIs, 26.3 %, 3 grafted mice), WT-2 (34 out of 34 ROIs, 100 %, 3 grafted mice) or TS21-2 (11 out of 23 ROIs, 47.8 %, 3 grafted mice) grafts that exhibit bursts at 3-5 mpt. Z-test, ****P* <0.001. (**P**) Frequency of burst events in WT-1, Ts21-1, WT-2 and Ts21-2 grafts measured at 3-5 mpt. Kruskal-Wallis test, ***P* < 0.01; ****P* < 0.001. (**Q**) Global ROI activity in WT-1, Ts21-1, WT-2 and

Ts21-2 grafts measured at 3-5 mpt. Kruskal-Wallis test, ***P <0.001. Scale bars, 10 μm [(A) and (B)], 5 μm [(E, left) and (J)], 2 μm (E, right), 0.2 μm (G), and 20 μm [(M), (N)].

Conclusion

We investigated the earliest stages of human axon, synaptic and network activity development in a complex genetic disorder by combining live imaging in a multi-structured tissue environment and patient-specific genetic background.

Transplanted human neurons continued to develop and mature *in vivo*, in a microenvironment that retained features reminiscent of human fetal cortex, such as the large size (up to ~100 mm^3 at 5 mpt, movie S1), temporal order and duration (i.e. many months) of neurogenesis (*20*), vascularization, cell diversification (human-derived cortical progenitors, neurons, oligodendrocytes and astrocytes together with host-derived microglia and vessels), as well as complex cytoarchitecture. However, the extent to which neurons in human cortical tissue grafts, either generated from human iPSCs (present study) or ESCs (*20, 38, 44*), can mimic the maturation, complexity and functionality of early human fetal cortical networks remains to be fully established.

Repeated imaging of single human neurons in cortical tissue grafts enabled us to gain insights on pruning, synaptic refinement, and functional neural network formation *in vivo*.
We found that pruning mainly occurred by branch-specific retraction, rather than degeneration.

Nascent human excitatory synaptic networks already had balanced rates of synaptic gain and loss over ~ one week at the single cell level, suggesting that immature human neurons possess intrinsic programs of synaptic turnover regulation over relatively short time scales. Human synaptogenesis and axon growth were concurrent, rather than happening at different times, confirming previous post-mortem static analysis (*28*), and revealing conservation of this developmental growth program between species (*45*).

Oscillatory population activity had marked neuropil and soma synchronization which became more prominent over 2 months, underscoring on-going modifications of cortical circuits. Results were robust across two independent control lines, providing a basis for applying this approach, which combines live imaging in a multi-structured tissue environment with patient-specific genetic background (*46*), to many other neurodevelopmental diseases affecting the cortex.

Here we modeled a complex genetic disorder and saw that while developmental axon refinement was normal, synapses were more stable and neural network activity was reduced in tissue grafts from two individuals with DS, suggesting a possible role for patterned activity in regulating synaptic lifetimes in the early stages of human cortical circuit development (*32*). These deficits were evident even after Ts21 cells were exposed to the *in vivo* physiological microenvironment of the mouse brain for several months, indicating cell-intrinsic deficits. Consistently, using a revertant disomic iPSC line we showed that the population activity deficits were rescued by the loss of an extra copy of Hsa21, indicating

that heightened expression of Hsa 21 genes is both necessary and sufficient to disrupt oscillatory burst activity in developing cortical DS networks *in vivo*.

In most previous work, human ESC or iPSCs-derived neurons have been transplanted in the damaged cortex (*38, 47*), spinal cord (*48*), striatum (*49, 50*) or retina (*51*), with the aim of cell replacement (*11*), rather than for disease modelling (*6, 52*), as demonstrated in our study. Transplantation and *in vivo* imaging for disease modelling in mice is advantageous compared to higher species such as primates, as larger numbers of animals can be used to track cells in the grafts over long periods of time, while providing a microenvironment containing vessels, immune cells and innervation, not present in common *in vitro* preparations.

In summary, we established a new *in vivo* experimental model of DS to study how the chromosomal abnormality affects the earliest stages of human axon, synaptic and functional neural network development. We expect this single-cell-resolution intravital microscopy approach will advance the knowledge of cellular pathophysiology in this and other neurodevelopmental disorders, particularly valuable in light of the scarcity of early human fetal brain tissue material.

References and Notes

1. W. M. Cowan, J. W. Fawcett, D. D. O'Leary, B. B. Stanfield, Regressive events in neurogenesis. *Science* **225**, 1258-1265 (1984).
2. L. K. Low, H. J. Cheng, Axon pruning: an essential step underlying the developmental plasticity of neuronal connections. *Philos Trans R Soc Lond B Biol Sci* **361**, 1531-1544 (2006).
3. Y. Herault *et al.*, Rodent models in Down syndrome research: impact and future opportunities. *Disease models & mechanisms* **10**, 1165-1186 (2017).
4. A. O'Doherty *et al.*, An aneuploid mouse strain carrying human chromosome 21 with Down syndrome phenotypes. *Science* **309**, 2033-2037 (2005).
5. M. Gupta, A. R. Dhanasekaran, K. J. Gardiner, Mouse models of Down syndrome: gene content and consequences. *Mamm Genome* **27**, 538-555 (2016).
6. I. Espuny-Camacho *et al.*, Hallmarks of Alzheimer's Disease in Stem-Cell-Derived Human Neurons Transplanted into Mouse Brain. *Neuron* **93**, 1066-1081 e1068 (2017).
7. J. van den Ameele, L. Tiberi, P. Vanderhaeghen, I. Espuny-Camacho, Thinking out of the dish: what to learn about cortical development using pluripotent stem cells. *Trends Neurosci* **37**, 334-342 (2014).
8. Y. Shi, P. Kirwan, J. Smith, H. P. Robinson, F. J. Livesey, Human cerebral cortex development from pluripotent stem cells to functional excitatory synapses. *Nat Neurosci* **15**, 477-486, S471 (2012).
9. M. A. Lancaster *et al.*, Cerebral organoids model human brain development and microcephaly. *Nature* **501**, 373-379 (2013).
10. P. Carmeliet, M. Tessier-Lavigne, Common mechanisms of nerve and blood vessel wiring. *Nature* **436**, 193-200 (2005).
11. L. H. Thompson, A. Bjorklund, Reconstruction of brain circuitry by neural transplants generated from pluripotent stem cells. *Neurobiol Dis* **79**, 28-40 (2015).
12. J. S. Barbosa *et al.*, Neurodevelopment. Live imaging of adult neural stem cell behavior in the intact and injured zebrafish brain. *Science* **348**, 789-793 (2015).
13. Y. Shi, P. Kirwan, F. J. Livesey, Directed differentiation of human pluripotent stem cells to cerebral cortex neurons and neural networks. *Nat Protoc* **7**, 1836-1846 (2012).
14. M. E. Emborg *et al.*, Induced pluripotent stem cell-derived neural cells survive and mature in the nonhuman primate brain. *Cell reports* **3**, 646-650 (2013).
15. X. Qian *et al.*, Brain-Region-Specific Organoids Using Mini-bioreactors for Modeling ZIKV Exposure. *Cell* **165**, 1238-1254 (2016).
16. A. Hoerder-Suabedissen, Z. Molnar, Development, evolution and pathology of neocortical subplate neurons. *Nat Rev Neurosci* **16**, 133-146 (2015).
17. T. Saito *et al.*, Neocortical layer formation of human developing brains and lissencephalies: consideration of layer-specific marker expression. *Cereb Cortex* **21**, 588-596 (2011).
18. N. Palomero-Gallagher, K. Zilles, Cortical layers: Cyto-, myelo-, receptor- and synaptic architecture in human cortical areas. *Neuroimage*, (2017).
19. I. M. Zakiewicz, J. G. Bjaalie, T. B. Leergaard, Brain-wide map of efferent projections from rat barrel cortex. *Front Neuroinform* **8**, 5 (2014).
20. I. Espuny-Camacho *et al.*, Pyramidal neurons derived from human pluripotent stem cells integrate efficiently into mouse brain circuits in vivo. *Neuron* **77**, 440-456 (2013).
21. L. Luo, D. D. O'Leary, Axon retraction and degeneration in development and disease. *Annu Rev Neurosci* **28**, 127-156 (2005).
22. A. Nikolaev, T. McLaughlin, D. D. O'Leary, M. Tessier-Lavigne, APP binds DR6 to trigger axon pruning and neuron death via distinct caspases. *Nature* **457**, 981-989 (2009).

23. C. Portera-Cailliau, R. M. Weimer, V. De Paola, P. Caroni, K. Svoboda, Diverse modes of axon elaboration in the developing neocortex. *PLoS Biol* **3**, e272 (2005).
24. V. De Paola *et al.*, Cell type-specific structural plasticity of axonal branches and boutons in the adult neocortex. *Neuron* **49**, 861-875 (2006).
25. V. De Paola, S. Arber, P. Caroni, AMPA receptors regulate dynamic equilibrium of presynaptic terminals in mature hippocampal networks. *Nat Neurosci* **6**, 491-500. (2003).
26. P. Caroni, F. Donato, D. Muller, Structural plasticity upon learning: regulation and functions. *Nat Rev Neurosci* **13**, 478-490 (2012).
27. T. L. Petit, J. C. LeBoutillier, D. P. Alfano, L. E. Becker, Synaptic development in the human fetus: a morphometric analysis of normal and Down's syndrome neocortex. *Exp Neurol* **83**, 13-23 (1984).
28. P. R. Huttenlocher, A. S. Dabholkar, Regional differences in synaptogenesis in human cerebral cortex. *J Comp Neurol* **387**, 167-178 (1997).
29. M. E. Molliver, I. Kostovic, H. van der Loos, The development of synapses in cerebral cortex of the human fetus. *Brain Res* **50**, 403-407 (1973).
30. A. Holtmaat *et al.*, Long-term, high-resolution imaging in the mouse neocortex through a chronic cranial window. *Nat Protoc* **4**, 1128-1144 (2009).
31. O. Garaschuk, J. Linn, J. Eilers, A. Konnerth, Large-scale oscillatory calcium waves in the immature cortex. *Nat Neurosci* **3**, 452-459 (2000).
32. R. Khazipov, H. J. Luhmann, Early patterns of electrical activity in the developing cerebral cortex of humans and rodents. *Trends Neurosci* **29**, 414-418 (2006).
33. P. Kirwan *et al.*, Development and function of human cerebral cortex neural networks from pluripotent stem cells in vitro. *Development* **142**, 3178-3187 (2015).
34. G. Quadrato *et al.*, Cell diversity and network dynamics in photosensitive human brain organoids. *Nature* **545**, 48-53 (2017).
35. T. W. Chen *et al.*, Ultrasensitive fluorescent proteins for imaging neuronal activity. *Nature* **499**, 295-300 (2013).
36. S. Vanhatalo *et al.*, DC-EEG discloses prominent, very slow activity patterns during sleep in preterm infants. *Clin Neurophysiol* **113**, 1822-1825 (2002).
37. P. J. Uhlhaas, F. Roux, E. Rodriguez, A. Rotarska-Jagiela, W. Singer, Neural synchrony and the development of cortical networks. *Trends Cogn Sci* **14**, 72-80 (2010).
38. A. A. Mansour *et al.*, An in vivo model of functional and vascularized human brain organoids. *Nat Biotechnol*, (2018).
39. C. Chen *et al.*, Role of astroglia in Down's syndrome revealed by patient-derived human-induced pluripotent stem cells. *Nature communications* **5**, 4430 (2014).
40. G. A. Maclean *et al.*, Altered hematopoiesis in trisomy 21 as revealed through in vitro differentiation of isogenic human pluripotent cells. *Proc Natl Acad Sci U S A* **109**, 17567-17572 (2012).
41. J. P. Weick *et al.*, Deficits in human trisomy 21 iPSCs and neurons. *Proc Natl Acad Sci U S A* **110**, 9962-9967 (2013).
42. K. Plona, T. Kim, K. Halloran, A. Wynshaw-Boris, Chromosome therapy: Potential strategies for the correction of severe chromosome aberrations. *Am J Med Genet C Semin Med Genet* **172**, 422-430 (2016).
43. E. Dossi, F. Vasile, N. Rouach, Human astrocytes in the diseased brain. *Brain research bulletin* **136**, 139-156 (2018).
44. K. Mollgard, J. J. Lundberg, B. K. Beebe, A. Bjorklund, U. Stenevi, The intracerebrally cultured 'microbrain': a new tool in developmental neurobiology. *Neurosci Lett* **8**, 295-301 (1978).
45. S. Falkner *et al.*, Transplanted embryonic neurons integrate into adult neocortical circuits. *Nature* **539**, 248-253 (2016).

46. J. A. Korecka, S. Levy, O. Isacson, In vivo modeling of neuronal function, axonal impairment and connectivity in neurodegenerative and neuropsychiatric disorders using induced pluripotent stem cells. *Mol Cell Neurosci* **73**, 3-12 (2016).
47. D. Tornero *et al.*, Synaptic inputs from stroke-injured brain to grafted human stem cell-derived neurons activated by sensory stimuli. *Brain* **140**, 692-706 (2017).
48. P. Lu *et al.*, Long-distance growth and connectivity of neural stem cells after severe spinal cord injury. *Cell* **150**, 1264-1273 (2012).
49. V. Tabar *et al.*, Migration and differentiation of neural precursors derived from human embryonic stem cells in the rat brain. *Nat Biotechnol* **23**, 601-606 (2005).
50. M. Wernig *et al.*, Neurons derived from reprogrammed fibroblasts functionally integrate into the fetal brain and improve symptoms of rats with Parkinson's disease. *Proc Natl Acad Sci U S A* **105**, 5856-5861 (2008).
51. M. Mandai *et al.*, Autologous Induced Stem-Cell-Derived Retinal Cells for Macular Degeneration. *N Engl J Med* **376**, 1038-1046 (2017).
52. H. Q. Huo *et al.*, Modeling Down Syndrome with Patient iPSCs Reveals Cellular and Migration Deficits of GABAergic Neurons. *Stem Cell Reports* **10**, 1251-1266 (2018).
53. M. A. Israel *et al.*, Probing sporadic and familial Alzheimer's disease using induced pluripotent stem cells. *Nature* **482**, 216-220 (2012).
54. I. H. Park *et al.*, Disease-specific induced pluripotent stem cells. *Cell* **134**, 877-886 (2008).
55. A. J. Peters, S. X. Chen, T. Komiyama, Emergence of reproducible spatiotemporal activity during motor learning. *Nature* **510**, 263-267 (2014).
56. L. Regeur, B. Pakkenberg, Optimizing sampling designs for volume measurements of components of human brain using a stereological method. *J Microsc* **155**, 113-121 (1989).
57. F. W. Grillo *et al.*, Increased axonal bouton dynamics in the aging mouse cortex. *Proc Natl Acad Sci U S A* **110**, E1514-1523 (2013).
58. A. Dubbs, J. Guevara, R. Yuste, moco: Fast Motion Correction for Calcium Imaging. *Front Neuroinform* **10**, 6 (2016).
59. S. J. Barnes *et al.*, Subnetwork-Specific Homeostatic Plasticity in Mouse Visual Cortex In Vivo. *Neuron* **86**, 1290-1303 (2015).
60. R. P. Sammons, C. Clopath, S. J. Barnes, Size-Dependent Axonal Bouton Dynamics following Visual Deprivation In Vivo. *Cell reports* **22**, 576-584 (2018).

Acknowledgments: We thank Drs. Kambiz Alvian, Richard Festenstein, Tara Keck and Madeline Lancaster for comments on the manuscript. Dr. Smaragda Papadoupoulou for help with immunohistochemistry. Cher Bass and Dr. Anil A. Bharath (Imperial College London) for help with the calcium imaging analysis. Chad Whilding for developing a customized FIJI script for image analysis. Maria Tortora for help with the immunohistochemistry experiments and analysis and Carla Pernaci for help with the analysis. Maksim Lavrov and Martyna Rakowska for help with synaptic dynamics analysis.

Emma Mustafa, Aleksandra Czerniak, Katie Horan, Aaron Matthews and Emma Rowley assisted with animal care and monitoring. Dr. Marco Tripodi (LMB, Cambridge) for the kind gift of the modified rabies transynaptic tracer. Prof. Gordon Stamp for the analysis of H&E stained material. **Funding:** Supported by the Medical Research Council (V.D.P.); GABBA PhD program (FCT fellowship PD/BD/52198/2013), the Rosetrees Trust and ARUK (R.R.); Wellcome Senior Investigator Award (F.J.L.) and the Alborada Trust of the ARUK Stem Cell Research Centre (M.P. and F.J.L.). **Author contributions:** V.D.P. conceived and planned the live imaging, characterization and analysis of transplanted patient-derived neuron experiments, and brought F.J.L. into the project; F.J.L. independently generated the iPSC-derived neurons, conceived the *in vitro* aspects of the project and contributed to the study design. R.R., A.T. and V.D.P. performed the grafting and the two-photon imaging experiments, analyzed the data, and prepared the related figures and text; M.P. performed the human iPSC-derived neuron differentiation and *in vitro* characterization, the copy number assay, the lentiviral vector transductions and provided input on the design of the experiments; R.R. and S.K. performed cell marker immunohistochemistry, imaging and analysis for the characterization of cell identity after transplantation, and prepared the relevant figures with input from V.D.P.; R.R. conducted and analyzed the whole-brain rabies tracing reconstructions. M.A.S. performed the electrophysiology recordings in acute brain slices containing the human grafts and prepared the relevant figure and text; S.J.B. analyzed the *in vivo* calcium imaging data and prepared the relevant figures and text with input from R.R. and V.D.P.; A.M. generated and characterized the Ts21-2, WT-2 and WT-2' lines with input from F.J.L.; A. S. analyzed the gene expression, CNV and STR data and prepared the relevant figures. J.D. and S.K. characterized the graft size; J.D. characterized

the axon projections from the grafts; E.V. provided input on the Hsa21 FISH experiment and analyzed the FISH data with input from V.D.P.; G.K. performed and analyzed the electron microscopy reconstructions and prepared the relevant figures. V.D.P. led the project; and V.D.P and R.R. wrote the paper with contributions from all authors. **Competing interests:** None. **Data and materials availability:** All data needed to evaluate the conclusion in the paper are present in the paper or the supplementary materials.

Supplementary Materials

Materials and Methods
Figs. S1 to S21
Table S1
Captions for Movies S1 to S6
References (53 to 60)

Supplementary Materials for

In vivo modeling of human neuron dynamics and Down syndrome

Raquel Real[1,2#], Manuel Peter[3#], Antonio Trabalza[1#], Shabana Khan[1], Mark A. Smith[1], Samuel J. Barnes[4], Ayiba Momoh[3], Alessio Strano[3], Joana Dopp[1], Emanuela Volpi[5], Graham Knott[6], Frederick J. Livesey[3,7*] and Vincenzo De Paola[1*]

*Corresponding author. Email: vincenzo.depaola@imperial.ac.uk; r.livesey@ucl.ac.uk

[#]These authors contributed equally to this work.

This PDF file includes:

Other Supplementary Materials for this manuscript includes the following:

Materials and Methods

Generation of iPSC cultures

Human stem cell research was approved by the Steering Committee for the UK Stem Cell Bank and for the Use of Stem Cell Lines. Skin biopsies were collected from donor individuals with Down Syndrome by the University of Cambridge Dept. of Psychiatry, following approval of the Cambridgeshire Research Ethics Committee, with informed consent from the donor or representative. Samples were designated anonymous identifiers following collection. Skin punch biopsies were subdivided and cultured at 37°C in 5% CO2 in DMEM + Glutamax (Thermo Fisher Scientific) supplemented with 10% foetal calf serum, penicillin (50 U ml−1), and streptomycin (50 µg ml−1) and 1 mM Sodium Pyruvate (Sigma) until fibroblast outgrowth was observed. When plates were confluent, fibroblasts were trypsinized and transferred to T75 dishes for further expansion. Cellular reprogramming of fibroblasts was carried out using Cytotune 2.0 Sendai Reprogramming kits (Thermo Fisher Scientific) according to the manufacturers protocol, and established using feeder free conditions in Essential-8 media (Thermo Fisher Scientific). Cells were grown in Essential-8 medium (Thermo Fisher Scientific) as feeder free cultures on Geltrex (Thermo Fisher Scientific) coated plates and maintained at 5% CO2 at 37°C in a humidified incubator.

Primary skin fibroblasts from a Ts21 donor were reprogrammed using non-integrative Sendai viruses and obtained clones showed high expression levels of the stem cell pluripotency factor Oct4 (Fig. S1C). Clones were genotyped for the presence of the extra copy of human chromosome 21 (Hsa21) using a Taq Man copy number assay with probes for APP and Down Syndrome Critical Region 1 (DSCR1), two genes located on Hsa21. All clones showed the presence of three copies of APP and DSCR1 indicating trisomism of Hsa21 (Fig. S1A). During this initial screen we also found one clone from the trisomic donor that was disomic for APP and DSCR1 indicating a loss of the extra copy of Hsa21 during the re-programming process. Throughout this study we further used published disomic control (WT-1, NDC1.2, non-demented control) (*53*) and trisomic human iPSCs (Ts21-1) (*54*) (Fig. S1A) and compared those to our trisomic/revertant disomic pair.

Directed differentiation of human iPSCs

Directed differentiation of iPSCs to cortical excitatory neurons was carried out as previously described (*8*). Briefly, 24 h before the start of differentiation iPSCs were passaged with 0.5 mM EDTA and plated at high density. Upon reaching 100% confluence the neuronal induction was started (Day 0). The medium was changed to neuronal maintenance medium supplemented with 10 µM SB431542 (Tocris) and 1 µM Dorsomorphin (Tocris) and was changed daily. On day 12 the neuroepithelial sheet was lifted off with Dispase (Thermo Fisher Scientific), broken up to small clumps and plated on laminin (Sigma) coated plates in neuronal maintenance medium supplemented with 10 µM SB431542 and 1 µM Dorsomorphin. On the next day (Day 13), the media was changed to neuronal maintenance medium supplemented with 20 ng ml^{-1} Fibroblast growth factor 2 (FGF2; PeproTech). Medium was changed every other day and FGF2 was removed from the medium on day 17. Cells were split with Dispase at a 1:2 ratio when neuronal rosettes started to meet. On day 25 cells were dissociated with Accutase (Thermo Fisher Scientific) and plated at a 1:1 ratio on laminin coated plates. Cell were

expanded 1:2 when they reached 90% confluence until day 33. On day 31-33 they were infected with high titer lentiviruses. Neurons were engrafted between day 36 and 38.

Neuronal maintenance medium (1 L) consisted of 500 ml DMEM:F12 + glutamax (Thermo Fisher Scientific), 0.25 ml Insulin (10 mg ml^{-1}, Sigma), 1 ml 2-mercaptoethanol (50mM Thermo Fisher Scientific), 5 ml non-essential amino acids (100 X Thermo Fischer Scientific), 5 ml Sodium Pyruvate (100 mM, Sigma), 2.5 ml Pens/Strep (10000 U/µl, ThermoFisher Scientific), 5 ml N2 (ThermoFisher Scientific), 10 ml B27 (Thermo Fisher Scientific), 5 ml Glutamax (100 X, Thermo Fisher Scientific) and 500 ml Neurobasal (Thermo Fisher Scientific) medium.

Copy number assay *in vitro*

Neurons were grown in neuronal maintenance medium, harvested with Accutase and genomic DNA was isolated with the DNeasy Blood & Tissue kit (Quiagen) following the manufacturers protocol. The presence of an extra copy of chromosome 21 was determined using a TaqMan copy number assay (Thermo Fisher Scientific) for APP (Hs01180853_cn, Thermo Fisher Scientific) and DSCR1 (Hs01114326_cn, Thermo Fisher Scientific) according to the manufacturers protocol using 5 µl genomic DNA.

Gene expression analysis *in vitro*

RNA was collected from day 35-36 cultures and profiled with a custom Nanostring gene expression panel of approximately 250 genes. After subtracting the maximum negative control probe counts, gene counts were normalized using the geometric mean of 6 positive control probes and of 7 housekeeping genes (CLTC, GAPDH, GUSB, PPIA, RPLP1, RPS15A, RPS9).

Western blot *in vitro*

Whole cell protein extraction was performed by lysis of cell pellets in RIPA buffer supplemented with protease inhibitors tablets (Roche) and phosphatase inhibitors (Thermo Scientific) before removal of the soluble fraction. Western blot analysis was carried out using the following antibodies: β-actin, anti-APP C-Terminal Fragment, Tuj1, Synapsin1 and PSD95.

Cell line identity verification

Genomic DNA was extracted from iPSC clones using DNeasy Blood & Tissue kit (Qiagen) following the manufacturers protocol and profiled with PowerPlex 16 HS Multiplex STR assay (Promega). Genotype of third allele in trisomy lines was extrapolated from electropherogram peak height.

Genome-wide copy number SNP assay

Genomic DNA was extracted from iPSC clones using DNeasy Blood & Tissue kit (Qiagen) following the manufacturers protocol and sent for SNP analysis using the Infinium HumanCytoSNP-12 platform (Illumina), except for the WT-1 sample, which was run on CytoSNP850K platform (higher density). Data was processed using GenomeStudio 2.0 and CNV-region-report-v2.1 (Illumina).

Lentiviral production

Third generation lentivirus was produced by calcium phosphate transfection of HeK293T cells with pBOB-Syn-GFP or pBOB-Syn-GCaMP6s-P2A-tdTomato plasmids and complemented with the packaging plasmids pRSV-Rev and pMDLg/pRRE and the VSVG envelope plasmid pMD2.G.

Animals

Adult immunodeficient mice (*n* = 57; 3-4 month-old; NOD-SCID gamma, Charles River, UK) were used for all *in vivo* imaging experiments. All mice were given access to food and water *ad libitum* and maintained in a 12-hour light-dark cycle. All procedures were conducted by researchers holding a UK personal license and conducted in accordance with the UK Animals (Scientific Procedures) Act 1986.

Craniotomy and human neuron transplantation

Cranial windows were surgically implanted over the somatosensory cortex as previously described (*30*). Mice were anaesthetized with ketamine-xylazine intraperitoneal injection (0.083 mg/g ketamine, 0.0078 mg/g xylazine) and then administered intramuscular dexamethasone (0.02 ml at 4 mg/ml), to reduce inflammation, and subcutaneous bupivacaine (1 mg/kg), a local anesthetic. A few drops of lidocaine (1 % solution) were applied on the skull surface prior to a ~5 mm diameter craniotomy being drilled over the somatosensory cortex. Neurons previously transduced (DIV 31) with a lentiviral vector (LV) carrying either a GFP or a calcium reporter gene under the neuron-specific Human Synapsyn-1 promoter (LV-hSyn-GFP and LV-hSyn-GCaMP6s-2A-tdTomato, respectively) were dissociated with 1 ml accutase enzyme mix (Sigma), centrifuged and washed at 1200 rpm in PBS, before being resuspended in 15-20 microliters of cortex buffer for cell counts.

We injected 20,000 cells in two sites spaced 0.5 mm apart (i.e. 40,000 cells in total in 1 μl) in the AP axis at coordinates: AP -1.8; L +2.8; V -0.5 mm from bregma (i.e. the somatosensory cortex barrel field) using a micro pump (UMP-3, World Precision Instruments, USA) and a microelectrode (< 50 μm at the tip).

A glass coverslip was then placed over the craniotomy and sealed with cyanoacrilic veterinary glue and dental cement. The exposed skull was subsequently covered in dental cement and a metal bar included on the top for positioning at the two-photon microscope stage. Mice were allowed to recover for 21 days before imaging.

Two-Photon imaging *in vivo*

A purpose built two-photon microscope (Prairie Technologies) equipped with a tunable coherent Ti:Sapphire laser (Coherent) and PrairieView acquisition software was used for all imaging experiments. Mice were anaesthetized with oxygen and isoflurane mix (0.6-1.5 %) and secured to the microscope stage with the head metal bar attached to a custom-built fixed support. Eye ointment (Lacri-lube) was applied to the eyes to prevent dehydration and the temperature was maintained at around 36 °C by a heating pad. An Olympus 4 X objective with a 0.13 numerical aperture (NA) was used to identify characteristic blood vessels to reliably relocate regions-of-interest (ROIs) at each imaging time point. Olympus 20 X (NA = 1.2), 40 X (NA = 0.8) and 60 X (NA = 0.9) water immersion objectives were then used to acquire several ROIs per animal (GFP: 75 x 75

μm field of view, 512 x 512 pixels for neurite imaging and 50 x 50 μm field of view, 1024 x 1024 pixels for synaptic imaging, 1 μm step size; GCaMP6-tdTomato: 300 x 300 μm field of view, 256 x 256 pixels, single plane). A pulsed 910 nm laser beam was used with typical power never exceeding 70 mW on the back focal plane.

For calcium imaging, mice were lightly anaesthetized and transduced cells were identified using the TdTomato signal at 1040 nm. Four minutes recording sessions were then acquired at 3 Hz with the 920 nm laser to excite GCaMP6s. GCaMP6-expressing neurons have been shown to display normal physiological properties including input resistance, resting membrane potential, input–output relationship, synaptic input maps, and normal synaptic plasticity (*55*). Moreover, we found no difference between GFP and GCaMP6s expressing human neurons in terms of their biophysical/synaptic properties (unpaired *t*-test, $P > 0.05$).

Electron microscopy

Immediately after the last imaging session, the mouse was perfused with a buffered solution of 2.5% glutaraldehyde and 2% paraformaldehyde. The brain was then removed and serial 60-micron thick sections cut tangentially to its surface at the region of the previous live imaging. The sections were then stained with heavy metals and embedded in resin. Blocks were made in the region of the graft area which was visible in the resin embedded sections. Thin sections were cut at 50 nm thickness and collected on single slot grids. These were further stained and imaged in a transmission electron microscope (Tecnai, FEI Company).

Correlated 2-photon-serial electron microscopy

We reconstructed 41 dendritic spines, which had been imaged previously *in vivo* on a Ts21-1 neuron. Immediately after the last imaging session, the mouse was perfused with a buffered solution of 2.5% glutaraldehyde and 2% paraformaldehyde. The brain was then removed and serial 60-micron thick sections cut tangentially to its surface at the region of the previous live imaging. These sections were then imaged again in the 2-photon microscope and laser marks burnt around the exact dendrites of interest. The sections were then stained with heavy metals and embedded in resin. Blocks were made around the visible laser marks and imaged using block face scanning microscopy (Gatan 3View and Zeiss Merlin scanning electron microscope). Serial images were taken of the regions of interest, and these were aligned using the FIJI software, and the dendrites and axonal boutons reconstructed using the TrakEM2 tools. The 3D structure of the reconstructed dendrite and presynaptic boutons (**Fig. 4F**) was created with Blender software (version 2.57; Blender Foundation, http://www.blender.org).

Electrophysiology

Coronal slices (350 μm) containing the somatosensory cortex (Bregma -0.3 to +1.4 mm) were maintained at room temperature (22-25ºC) in an external solution containing (in mM) NaCl 125, KCl 2.5, NaH_2PO_4 1.25, $NaHCO_3$ 25, $CaCl_2$ 2, $MgCl_2$ 1, D-glucose 10, D-mannitol 15, equilibrated with 95% O_2, 5% CO_2, pH 7.4. Human neurons were visualized in the somatosensory cortex by the expression and excitation of GFP. Whole-cell current-clamp (I_{fast}) and voltage-clamp recordings were made at ~35 °C using borosilicate glass pipettes (4-8 MΩ) containing (in mM) Kgluconate 130, KCl 10, EGTA

0.5, NaCl 1, $CaCl_2$ 0.28, $MgCl_2$ 3, Na_2ATP 3, GTP 0.3, phosphocreatine 14 and HEPES 10 (pH 7.2). Neurons were also voltage-clamped at -70 mV using a modified internal solution in which Kgluconate was replaced with CsCl (130 mM). Slices were bathed in (+)-bicuculline (20 µM) for miniature excitatory currents (mEPSC) or NBQX for miniature inhibitory currents (mIPSC). For anatomical inspection, Lucifer-yellow-CH (1 mg/ml) was added to the internal electrode solution. Following access to the whole-cell configuration, Lucifer-yellow was allowed to dialyze the neuron for 10-15 minutes before gradually withdrawing the patch electrode from the cell. Slices were fixed in 4% (w/v) paraformaldehyde and permeabilized in PBS containing 0.4% (v/v) Triton-x and 2% (v/v) chicken serum. Slices were incubated with a rabbit anti-Lucifer-yellow antibody for 2-3 days at 4 °C and then incubated with a chicken anti-rabbit antibody conjugated with Alexa-594. Slices were mounted on glass coverslips prior to 2-photon imaging. Synaptic kinetic analysis was performed only on cells with at least 40 recorded events.

Immunohistochemistry, histology and related analysis

Neurons *in vitro* were washed with PBS and fixed with 4% PFA for 10 minutes, then blocked in a 5% normal goat serum in TBS + 0.3% Triton X-100 solution, incubated overnight with primary antibodies (**Supplementary Table 1**), and with the appropriate Alexa-dye conjugated secondary antibodies (1:500, Thermo Fisher Scientific) diluted in TBS + 0.3% Triton X-100. 4',6-Diamidino-2-Phenylindole (DAPI, 5 µg/ml final concentration) was used for nuclear counterstaining. Imaging was performed on an inverted Leica TCS SP8 scanning confocal microscope (Leica Microsystems). 4 µm image stacks were acquired and the z projection was used for counting cells using a custom automated ImageJ (NIH) script.

At the end of the live imaging experiments, animals were anesthetized with an overdose of ketamine and xylazine, and then perfused intracardially with PBS followed by 4% paraformaldehyde (PFA). Brains were fixed overnight in 4% PFA. Coronal brain sections were cut at 40 µm in a vibratome (Leica VT1000S) and stored free-floating in PBS with 0.01% NaN_3. For the cellular characterization of the grafts, consecutive sections containing the graft were blocked in a 10% donkey serum with 0.5% Triton X-100 PBS solution, and then incubated overnight with primary antibodies (**Supplementary Table 1**). Sections were then incubated with appropriate secondary antibodies (1:1000, Alexa Fluor®, Thermo Fisher Scientific). All incubations were performed in 5% donkey serum with 0.1% Triton X-100 PBS solution. When using primary antibodies raised in mouse and rat in the same tissue sections, primary and secondary antibody incubations were performed sequentially to avoid the anti-rat secondary antibody cross-reacting with mouse immunoglobulins. Sections were mounted using ProLong® Gold Antifade Mountant (Thermo Fisher Scientific). All sections stained with anti-NuMA antibody required a sodium citrate (10 mM, pH 6) heat-mediated antigen retrieval procedure. Brain sections were imaged with either a scanning confocal TCS SP5 II or SP8 microscope (Leica Microsystems), using a 20 X (NA 0.75) or oil-immersion 40 X objective (NA 1.45). ROIs were randomly selected within the graft area. A customised semi-automated script was used to analyze images with nuclear markers in FIJI. Briefly, nuclei were segmented and intensity values of segmented objects measured across all channels after background subtraction. Threshold levels were set to define positive objects. The criteria for threshold selection was elimination of type I error while

minimising the occurrence of type II error (<10%). Astrocytes (GFAP+) and oligodendrocyte progenitors (PDGFRα+) were manually counted in FIJI. Microglia was analysed using a custom Cell Profiler pipeline (Bloomfield et al, *in press*).

For the volumetric assessment of the graft, ROIs were drawn around human-specific Neural Cell Adhesion Molecule (hNCAM)-labelled human graft and each of their areas measured from every second consecutive coronal mouse section (total 48 sections, 140 μm apart) in ImageJ. Volume was calculated from the sum of areas, section thickness, and interval, according to Cavalieri's principle (*56*), and independently confirmed with *Imaris* image analysis software (Bitplane).

Teratoma formation was excluded and vascularization confirmed (20 out of 20 grafts) by inspection of H&E stained material by an expert pathologist.

For mapping axonal projections at 5 mpt, sections at 120 μm intervals were selected across the entire brain (n = 3), and immunostained for hNCAM (Supplementary Table 1) as above. All sections were imaged with an epifluorescence microscope (Olympus IX70) using a 20 X objective (NA 0.5, 0.321 μm pixel size). The Allen Mouse Brain Atlas (Paxinos and Franklin, 2001) was used to identify brain areas of interest. Image analysis was performed by manual counting of fibers using ImageJ. A color scheme with a range from grey (no projections) to bright red (more than 100 projections) was used to indicate the relative amount of axonal projections in each brain area.

Retrograde trans-synaptic tracing

TVA expressing lentivirus was produced as described previously using the pBOB-SYN-HTB plasmid (Addgene plasmid # 30195). Neurons were infected with the lentivirus expressing rabies glycoprotein (G), TVA and nuclear GFP (LV-hSyn-G-TVA-NLS-GFP) at day 30. The medium was changed the next day to remove the virus and neurons were stereotactically injected into the somatosensory cortex of adult NSG mice, as previously described. After 5 months, an EnvA-pseudotyped, G-deleted mCherry expressing rabies virus (EnvA + RV*dG*-mCherry) was injected in the same location. Animals were perfused 7 days later with 4% PFA intracardially, and the brains fixed overnight in 4% PFA. Coronal brain sections were cut at 50 μm in a vibratome, and stained with anti-human nuclei (hNu), anti-GFP and anti-DsRed antibodies (Supplementary Table 1), as described above. All regions of interest containing mCherry positive cells throughout the whole brain were imaged with a confocal Leica SP5 microscope using a 20 X objective (NA 0.7), and quantifications of mCherry+/hNu+ and mCherry+/hNu- input cells were performed by manual counting using ImageJ.

Fluorescence In Situ Hybridization (FISH) and analysis

Brain sections (40 μm) were dehydrated in ethanol series (30%, 50% and 70%). Sections were allowed to air dry at room temperature for 1 day, re-hydrated in PBS and then permeabilised in PBS with 0.5% Triton X-100. A heat-mediated step with sodium citrate buffer (10 mM, pH 6) was performed. Slides were transferred to 2x SSC, and afterwards equilibrated in a 2x SSC with 50% formamide solution for at least 4 hours, at room temperature. After applying the Hsa21 probe (XL 21q22/XCP 21, Metasystems), a coverslip was sealed with rubber cement and then slides were allowed to rest for 1h at room temperature, to allow probe penetration in the section. Slides were incubated at 80 °C for 5 minutes and then at 37 °C in a dark humidified chamber for 2 days, to allow

hybridization to occur. Slides were washed in 2x SSC at 37 °C, and then counterstained with DAPI (1:1000, Thermo Fisher Scientific). Sections were mounted using ProLong® Gold Antifade Mountant (Thermo Fisher Scientific) and imaged with a Leica SP5 confocal laser scanning microscope using an oil-immersion 63 X (NA 1.45) objective, z-stack range of 5-18 planes.

Analysis was carried out manually in 3D. Cell nuclei within Z-stacks obtained by confocal microscopy were individually evaluated and annotated blind to genotype using ImageJ (NIH). Nuclei that appeared to be either truncated or damaged, or overlapped with other nuclei, or showed significant background 'noise' were not included in the scoring. A minimum of 50 nuclei from a minimum of two different Z-stacks were evaluated for each line. Based on the observed number of fluorescent hybridization signals, nuclei were assigned to four different categories, namely 'one signal', 'two signals' 'three signals' and '> three signals'. Data gathered by FISH analysis on histological sections of grafts originating from euploid lines indicated that the assay met the sensitivity and specificity parameters generally recommended for FISH testing, >95% and >98% respectively (358 nuclei analyzed in total). On histological sections of grafts originating from Down syndrome cell lines, the presence of an extra copy of chromosome 21 was confirmed by evaluating the frequency of the triple fluorescent pattern ('three signals' nuclei/total nuclei) and by comparing it to the specific cut-off threshold values calculated from the normal reference ranges (*CRITBINOM,* 95% Confidence Level).

Data Analysis

Neurite length quantification. Image stacks from *in vivo* two-photon images were processed with Image J (section alignment, background subtraction, brightness and contrast adjustment). Neurites were then manually traced from a clear reference point in the maximum intensity projections for length measurement.

Dendritic spine/bouton dynamics. Quantifications were made at 3-4 mpt. Dendritic spine/bouton density was determined by blindly annotating dendritic spines/boutons in Matlab using custom made software (*57*) and metrics calculated in the following way:

• Total number of boutons/spines reported in the text and figure legends were calculated as the total number in the first session plus the number of gains across all imaging sessions (i.e. each synaptic structure was counted only once).

• Density of boutons/spines at any given time point a was defined as Density(a) = $n_a/length_a$.

• Turnover rate (TOR) was defined as (nG + nL)/(2*N), where nG and nL are the numbers of bouton/spine gains and losses respectively, and N is the total number of boutons/spines present in the same time interval. These total numbers include repeated counts of the same boutons/spines, in case they were present in more than one session.

• Gains and losses fractions between session a and b were defined as Gains(a; b) = $nG_{(b-a)}/N_{(a+b)}$ and Losses(a; b) = $nL_{(b-a)}/N_{(a+b)}$. N includes repeated counts of the same boutons/spines, in case they were present in more than one session.

• Survival fraction (Fr) was defined by the cumulative sum of EPBs/spines that survive at each time point (t), divided by the total number of EPBs/spines that were present at session 1:

$$Fr(T) = \left[\sum_{t=1}^{T} n_t\right]/n_1$$

***In vivo* calcium imaging**. Time-series were pre-processed in ImageJ using the moco plugin for registration (*58*), followed by the application of a 3D median filter (2 x 2 x 2, in x-y-z, respectively).

Analysis of sparse calcium activity. Neurons were selected based on the mean normalized maximum intensity projection of the data by hand and the nucleus was excluded from selection. Fluorescence traces were calculated as the average fluorescence of pixels lying within the cell in each frame. To remove slow changes in raw fluorescence traces, the 15th percentile value of the fluorescence distribution was subtracted from the raw fluorescence signal. $\%\Delta F/F_0$ signals were calculated by dividing the raw fluorescence signal by the median of each cells fluorescence distribution and normalizing to the background calcium signal. Cellular activity was calculated using the integrated fluorescence as describe previously (*59*) with a 15% $\Delta F/F_0$ threshold. Activity was then normalized to the duration of our imaging paradigm to give values in $\%\Delta F/F_0$/second, as described previously (*60*).

Burst activity analysis. We defined bursts as global events where > 95% of the peak pixel intensity was above the threshold defined above, across each imaged cortical area. All regions were then visually inspected to further validate the presence of global events.

Global activity analysis. Global analysis was the same as that for sparse activity, but for this analysis activity was measured over the entire region of interest.

Burst direction. For each event we calculated the peak of the first derivative of the $\%\Delta F/F_0$ transient at 8 spatial positions (based on breaking the image into a 3 x 3 grid and excluding the central square) in the imaged cortical region. We then took the time of the peak derivative value at each of the 8 spatial positions during a calcium event. Polar plots were calculated by taking the difference of each time-point from the earliest time-point, thus generating lag values for each of the 8 spatial positions. We then averaged lag values over all the events in the imaged region (10 – 40 events). We calculated the direction selectivity index (DSI) for each region as follows: $1 - R_{null}/R_{best}$, where R_{best} is the interpolated response to the direction with the longest lag and R_{null} is the interpolated response to the position opposite the direction with the longest lag. Regions of interest with a DSI value > 0.3 where considered to have a burst direction. Directionality of calcium bursts was not due to scanning artefacts as it did not always follow scanning direction.

Whisker stimulation responses. Following visual inspection of average $\% \Delta F/F_0$ calcium data, we found that 1 out of 3 animals exhibited time-locked responses to whisker stimulation. To examine whether these responses were indeed sensory driven or attributable to the contaminating effects of burst activity we developed a simple metric. A trial was considered to be driven by sensory stimulation if it had no response in a ten second baseline period, and a clear transient time locked to the onset of the whisker stimulation. To test how often our metric gave a false positive, we used randomly selected epochs of spontaneous activity that were matched in duration to our sensory stimulation trials as a control.

Statistical analyses were performed in GraphPad Prism V7 and SigmaPlot V13. All measurements are given as the mean ± standard error of the mean (SEM), unless otherwise stated. Results were considered significant when $P < 0.05$. The normality test used was the

Shapiro-Wilk test. Figures were prepared using Adobe Photoshop and Illustrator. Images in figures 1G, 1H, 1I, 1I', 1J, 2B (bottom panel), 2G, 2H, 4A, 4E, 4J and S20 are best projections in x-y-z of neuronal, dendritic or axonal stacks. Movies S4-6 were processed with mean 3D filtering and shown at the indicated frame per second (fps).

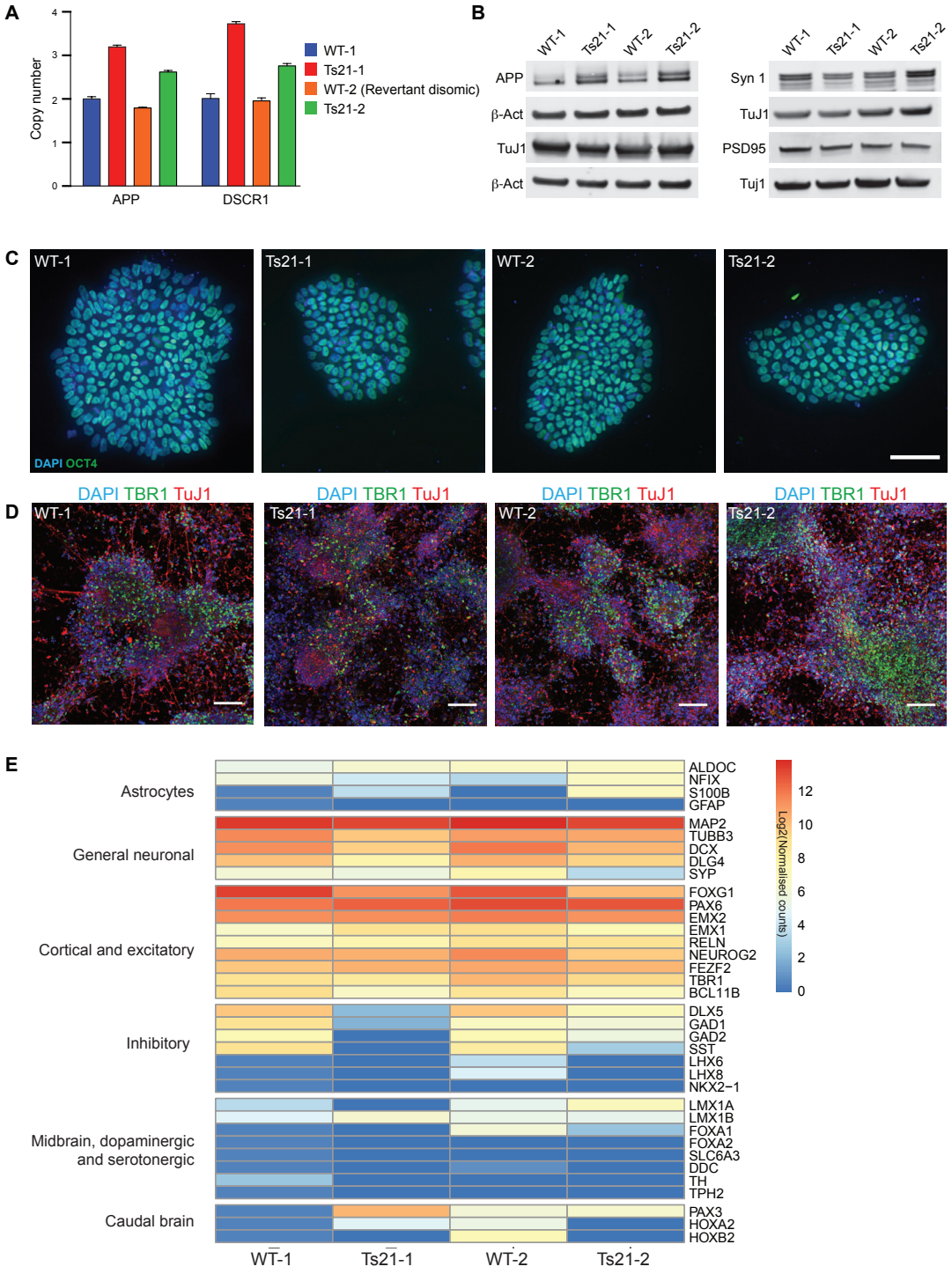

Figure S1. Characterization of human iPSC lines. (**A**) TaqMan copy number assay for APP and DSCR1in control and Ts21 neurons. Trisomic neurons have an extra copy of APP and DSCR1. WT-2 is a revertant disomic cell line from Ts21-2. (**B**) Western blot detection of APP, Tuj1, Syn1 and PSD95 at day 58. Ts21 neurons show normal levels of Tuj1, Syn1 and PSD95 but increased levels of APP compared to control neurons. (**C**) Re-programmed human iPSCs express the stem cell self-renewal factor OCT4. Scale bar, 50

μm. (**D**) Confocal image stacks of Ts21 and control neurons at day 50 immunostained for the neuronal marker Tuj1 and the deep layer marker TBR1. Scale bars, 100 μm. (**E**) Gene expression analysis of day 35-36 cultures. Heatmap of log2 normalised counts for selected genes expressed in the indicated brain regions and/or cell types. Note selective cortical identity. Each column of the heatmap is one sample run once.

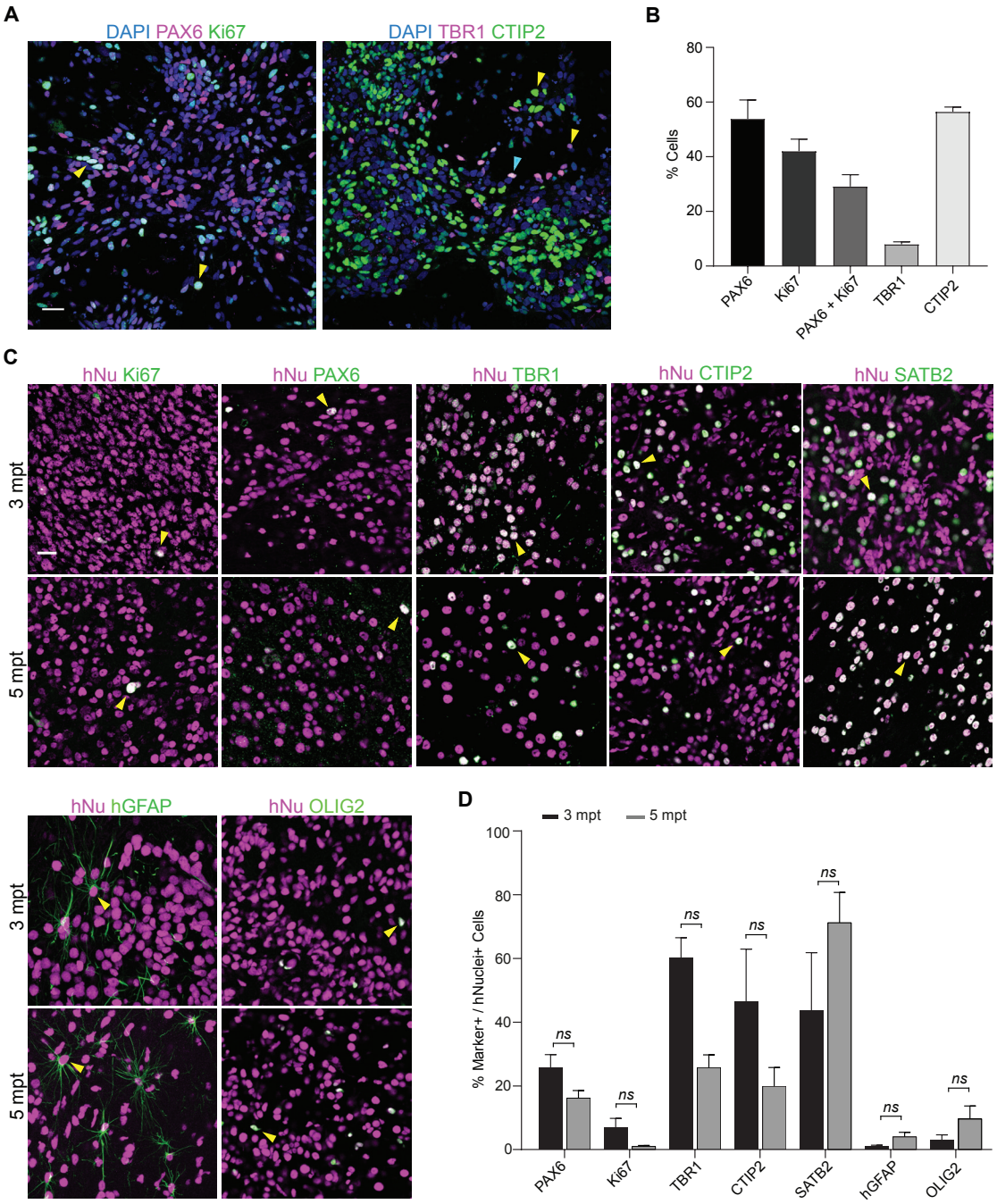

Figure S2. Maturation of diverse cell types in human tissue grafts. (**A**) Representative immunostaining at 36 days post-differentiation of human iPSC-derived neurons for DAPI, PAX6 (neuronal progenitor marker), Ki67 (proliferation marker), TBR1and CTIP2 (deep cortical layer markers). Yellow arrowheads indicate examples of proliferating neural progenitor cells (PAX6+/Ki67+, left) and neurons with deep layer identity (either CTIP2+ or TBR1+, right) and light blue indicates an example of a CTIP2+/TBR1+ nucleus. Scale bar, 30 µm. (**B**) Quantification of cell populations *in vitro* at day 36 post-differentiation (*n* = 4 wells). (**C**) Representative immunostaining of human grafts 3 and 5 months after transplantation for hNu (human nuclei marker), Ki67, PAX6, TBR1, CTIP2, SATB2

(upper cortical layer marker), Glial Fibrillary Acidic Protein (hGFAP, human astrocytic marker) and Oligodendrocyte Transcription Factor 2 (OLIG2, oligodendrocyte marker); arrowheads indicate examples of positive human cells. Scale bar, 20 μm.
(**D**) Quantification of cell populations *in vivo* at 3 and 5 mpt ($n = 3$ animals for each time point; hNu+ nuclei sampled per cell marker: 2994 ± 487 and 3283 ± 245 at 3 and 5 mpt respectively, mean ± SD). Sidak's multiple comparison test after one-way ANOVA; *ns*, not significant. Data are represented as mean ± SEM.

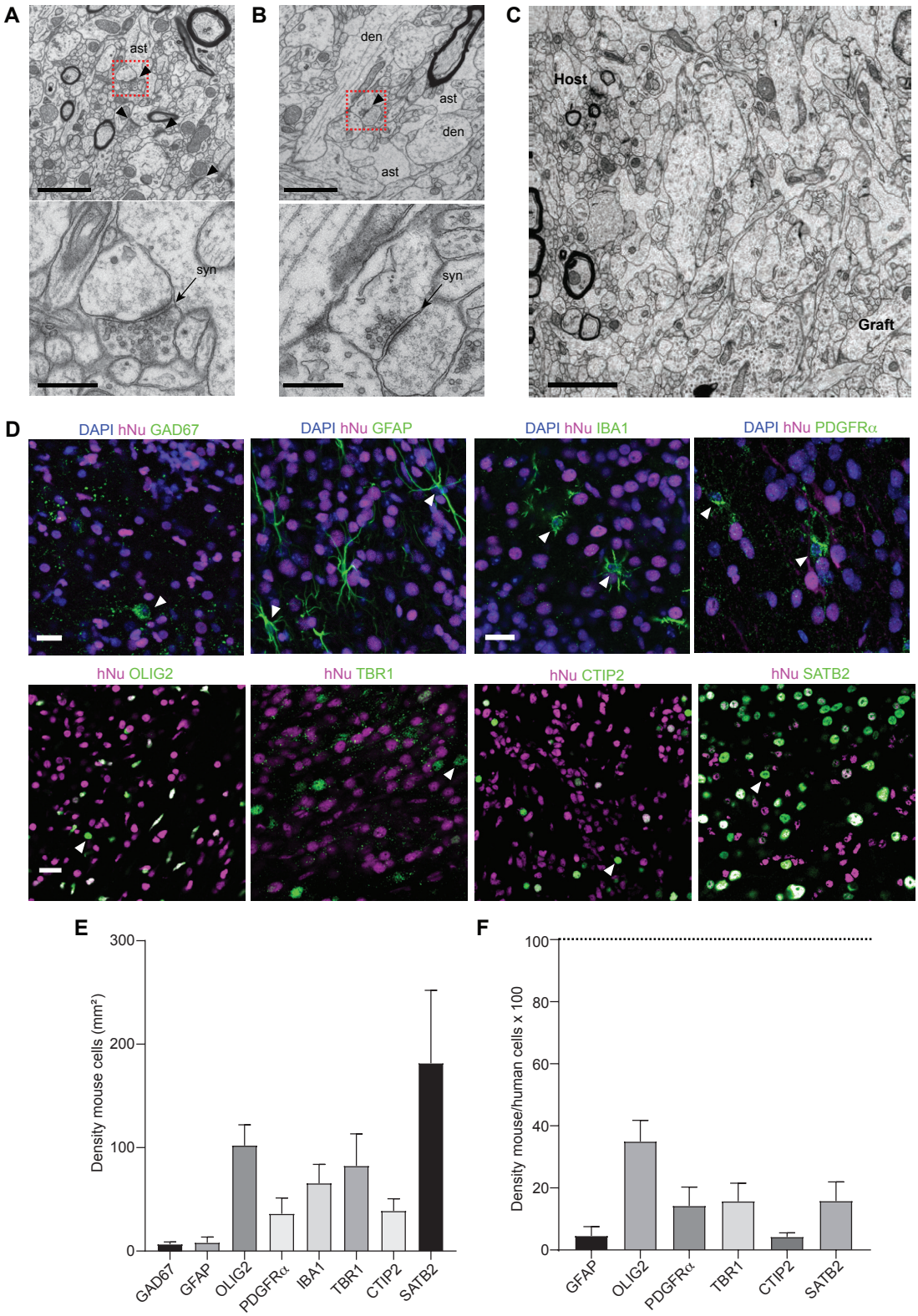

Figure S3. Graft ultrastructure and host-derived cell identity. (**A**) Representative electron microscopy image of neuropil of mouse cortex immediately adjacent to the graft.

A number of synapses (arrowheads) are present. The bottom panel is a magnified image of the region highlighted by the red box. Scale bars, 2 μm (top) and 0.5 μm (bottom). (**B**) Representative electron microscopy image of the human graft. Fewer synapses are present (enlarged example in bottom panel). ast, astrocytic profiles. den, dendrite. syn, synapse. Scale bars, 2 μm (top) and 0.5 μm (bottom) (**C**) Representative electron microscopy image of the interface between the human graft and the host brain tissue. Scale bar, 3 μm. (**D**) Representative immunostaining of human grafts 5 mpt for glutamic acid decarboxylase 67 (GAD67, inhibitory interneuron marker), platelet-derived growth factor receptor α (PDGFRα, oligodendrocyte precursor marker), ionized calcium-binding adapter molecule 1 (Iba1, microglia marker), GFAP, OLIG2, TBR1, CTIP2 and SATB2. Arrowheads indicate examples of positive mouse cells. Scale bar, 20 μm. (**E**) Quantification of mouse cell density in the graft (n = 3 mice; area sampled per cell marker: 1.54 ± 0.03 mm^2, mean ± SD). (**F**) Mouse cell density in the graft normalized to the respective human cell density (dashed line; n = 3 mice; area sampled per cell marker: 0.80 ± 0.08 mm^2, mean ± SD).

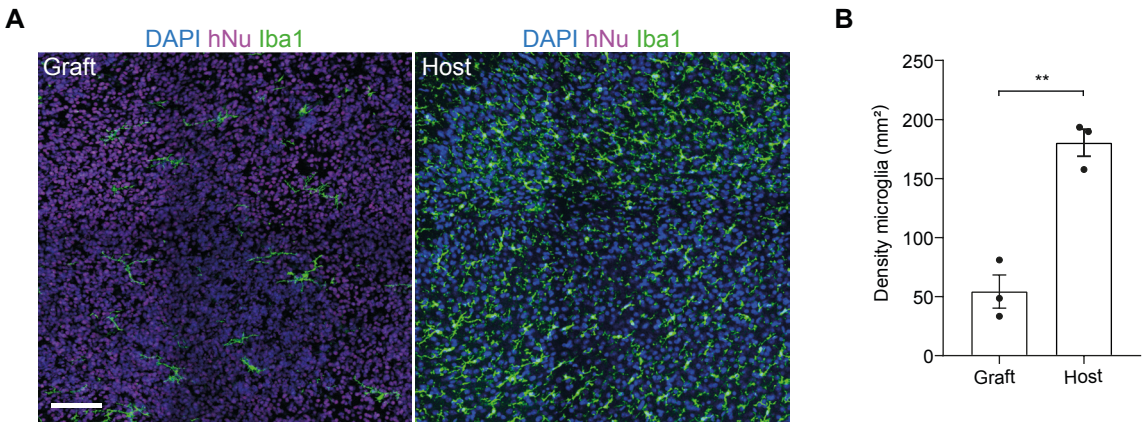

Figure S4. Minimal recruitment of mouse-derived microglia in the human tissue graft. (**A**) Representative example of Iba1/hNu staining at 3 mpt. Scale bar, 100 µm. (**B**) Quantification of microglia density at 3 mpt (n = 3 mice) in the graft (area sampled: 5.2 ± 1.5 mm^2, mean ± SD) and respective contralateral host cortex (area sampled: 2.4 ± 0 mm^2, mean ± SD). Paired t-test, $^{**}P < 0.01$. Each data point represents an animal.

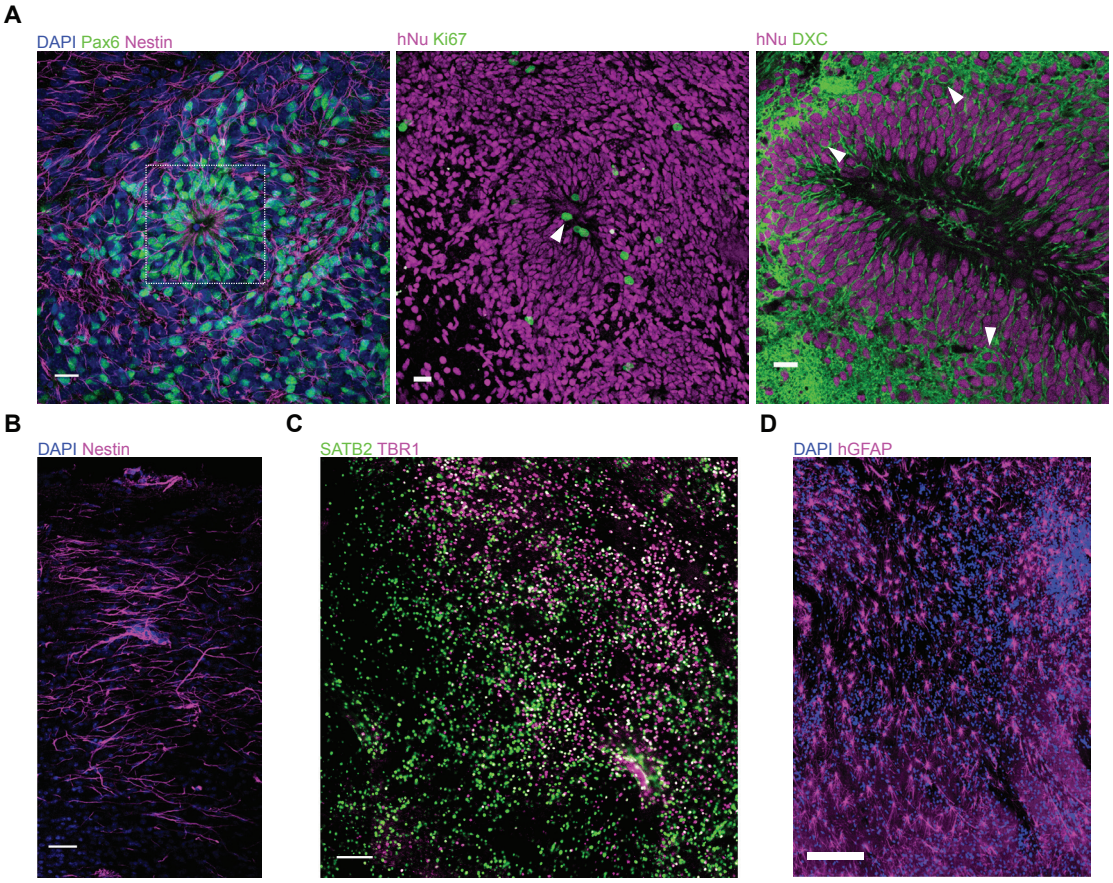

Figure S5. Complex cytoarchitecture in human cortical tissue grafts.
(**A**) Representative immunostaining of neural rosette-like structures in the human tissue grafts 2 mpt for PAX6, Nestin (radial glia marker), Ki67 and doublecortin (immature neuronal marker, DXC); arrowheads indicate examples of positive human cells. The highlighted region in the first image depicts the core of the neural rosette at its centre. Scale bars, 20 µm. (**B**) Representative immunostaining of Nestin-positive processes at 2 mpt. Scale bar, 50 µm. (**C**) Representative immunostaining of the human grafts at 5 mpt for TBR1 and SATB2. Scale bar, 100 µm. (**D**) Representative immunostaining of the human graft for hGFAP at 5 mpt. Note the homogeneous distribution of human astrocytes. Scale bar, 200 µm.

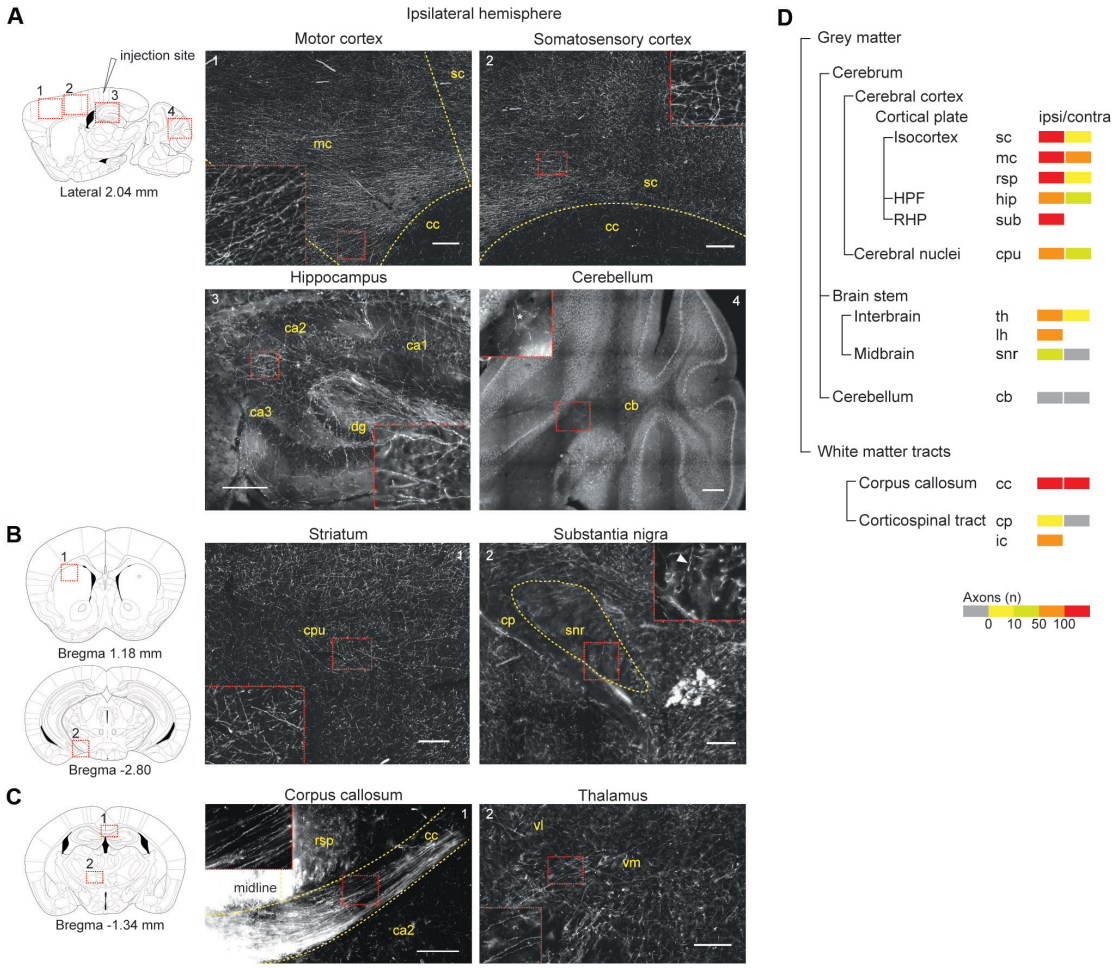

Figure S6. Human neurons project to known SCx1 targets. (**A**), Schematic sagittal view of the adult mouse brain (left). Numbered red boxes indicate: (1) somatosensory cortex adjacent to the injection site, (2) motor cortex, (3) hippocampus, and (4) cerebellum. Representative immunostaining of the numbered regions shown in the schematic for hNCAM (neuronal marker) at 5 mpt (right). Asterisk marks autofluorescence in a vessel. (**B**), Schematic coronal view of the adult mouse brain 1.18 (top left) and -2.80 mm (bottom left) from Bregma. Representative hNCAM immunostaining of the striatum, substantia nigra and cerebral peduncle at 5 mpt (right). Arrowhead in the inset shows an example of axon fiber. (**C**), Schematic coronal view of the adult mouse brain 1.34 mm from Bregma (left). Numbered red boxes indicate: (1) corpus callosum and (2) thalamus. Representative immunostaining of the regions indicated in the schematic for hNCAM at 5 mpt (right). Schematic brain images adapted from Paxinos and Franklin, 2001. Dashed yellow lines mark anatomical boundaries. Red dashed boxes contain magnified insets of images. Scale bars, 200 µm (A, B, C). (**D**), Quantification of axonal density in grey and white matter brain regions (n = 3 animals). Fiber density is color-coded (from grey: no human axons, to bright red: more than 100 human axons). mc, motor cortex; sc, somatosensory cortex; rsp, retrosplenial cortex; HPF, hippocampal formation; hip, hippocampal region; ca1, ca2, ca3 indicate CA1, CA2, CA3 subfields of hippocampus, respectively; dg, dentate gyrus; RHP, retrohippocampal region; sub, subiculum; cpu, caudate-putamen (striatum); th, thalamus; lh, lateral

hypothalamus; snr, substantia nigra; cb, cerebellum; cc, corpus callosum; cp, cerebral peduncle; ic, internal capsule; vl, ventrolateral thalamus; vm, ventromedial thalamus.

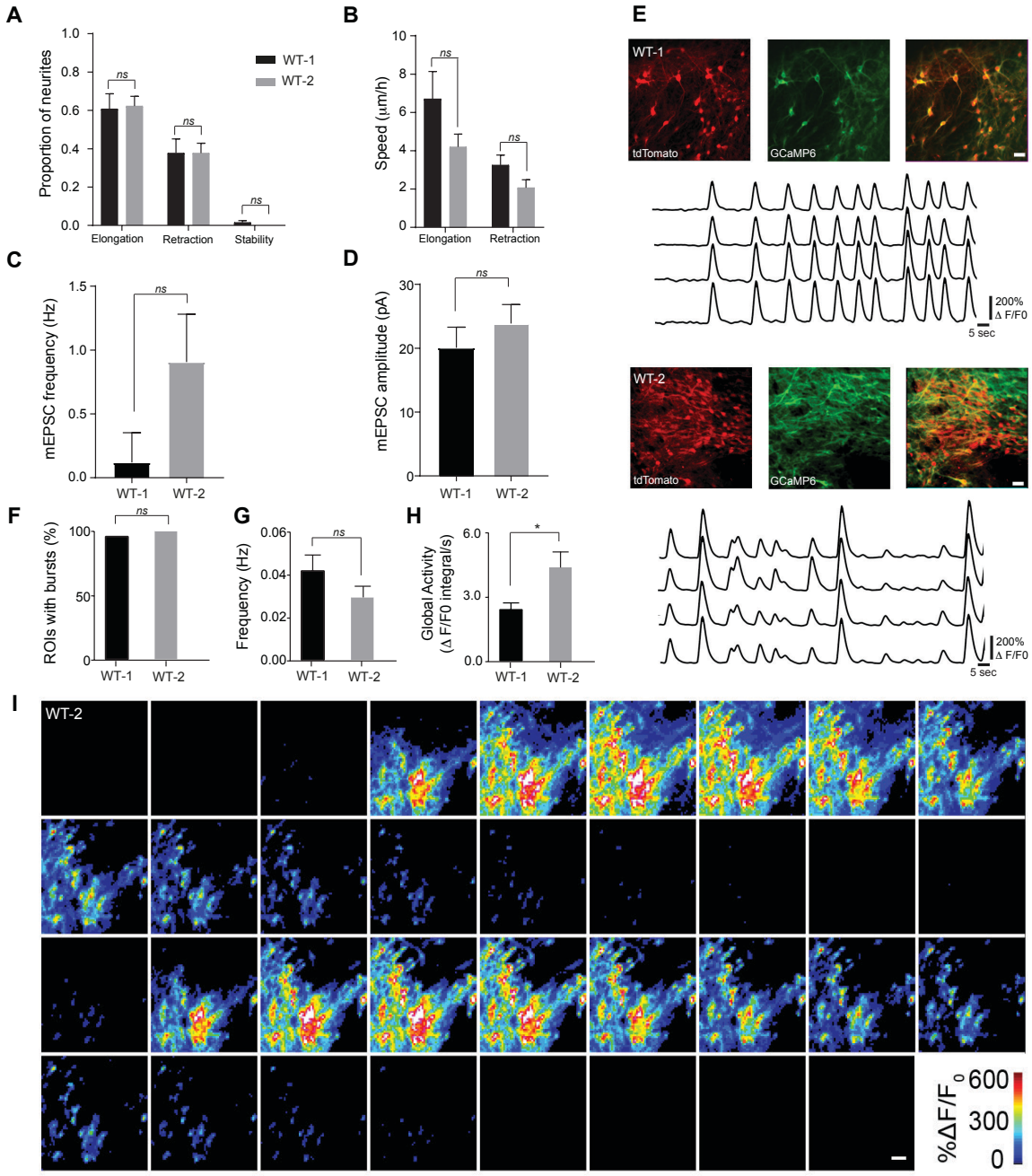

Figure S7. Reproducible human neuron dynamics in cortical tissue grafts from two independent control iPSC lines.

(**A**) Quantification of the proportion of neurites elongating, retracting and stable in 24h intervals at 3 wpt from WT-1 (n = 96 neurites from 79 cells in 7 animals) and WT-2 (n = 65 neurites from 53 cells in 4 animals) grafts. Unpaired two-tailed t-test, P = 0.2401 (elongation), P = 0.0510 (retraction). (**B**) Quantification of the speed of neurite elongation and retraction at 3 wpt in WT-1 (n = 96 neurites from 73 cells in 7 animals) and WT-2 grafts (n = 53 neurites from 43 cells in 4 animals). Two-way ANOVA, interaction $F_{6,54}$ = 0.3626, P = 0.8993. (**C**, **D**) Frequency and amplitude of mEPSC recorded at 5 mpt in WT-1 (n =18 cells from 4 animals) and WT-2 (n = 23 cells from 4 animals) grafts. Unpaired two-tailed t-test, P = 0.4237 (amplitude). Mann-Whitney U-

test, $P = 0.8812$ (frequency). (**E**) Example of burst activity and representative $\Delta F/F_0$ calcium traces from 4 active neurons in WT-1 and WT-2 grafts. Scale bar, 20 µm. (**F**) Percentage of ROIs in WT-1 (49/51 ROIs, 96 %) and WT-2 (33/33 ROIs, 100 %) grafts exhibiting spontaneous bursting activity. Z-test, $P = 0.662$. (**G**) Frequency of burst events in WT-1 and WT-2 at 3-5 months. Mann-Whitney *U*-test, $P = 0.376$. (**H**) Global activity for WT-1 vs WT-2 grafts at 3-5 months. Mann-Whitney U-test, $^*P < 0.05$. (**I**) Montage of image frames from a typical recurrent burst in a WT-2 graft at 112 dpt. Montage taken from movie S5. Scale bar 20 µm. Data are represented as mean ± SEM. *ns*, not significant.

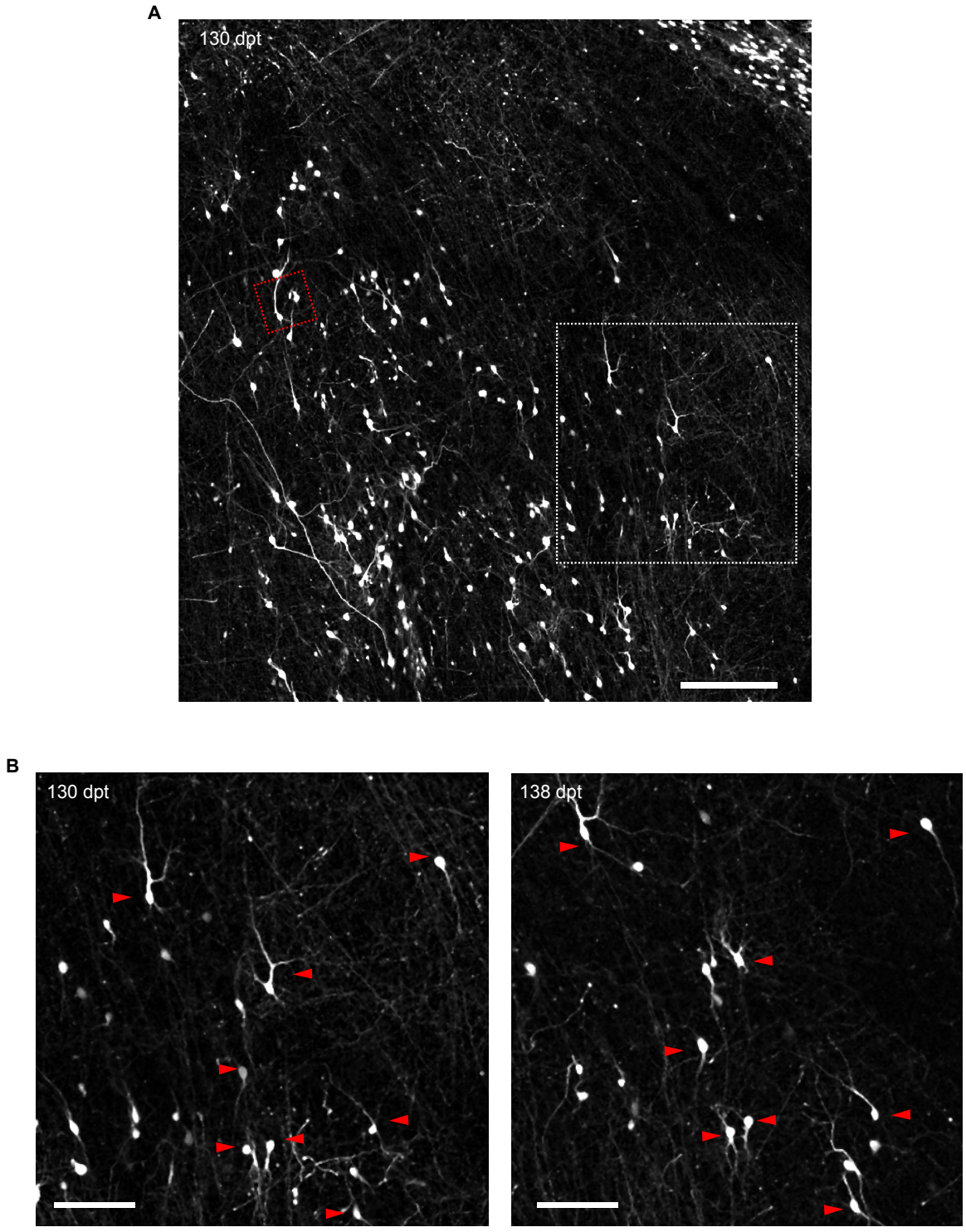

Figure S8. *In vivo* tracking of transplanted WT human neurons over 8 days.
(**A**) 2-photon *in vivo* imaging of a WT-1 graft at 130 dpt. Red box indicate same area as in fig. 2B, top panel. Scale bar, 200 µm. (**B**) Imaging of the same graft area (white box in (A)) over the indicated time. Red arrows represent examples of cells with a stable location over a 8-day period. Scale bars, 100 µm.

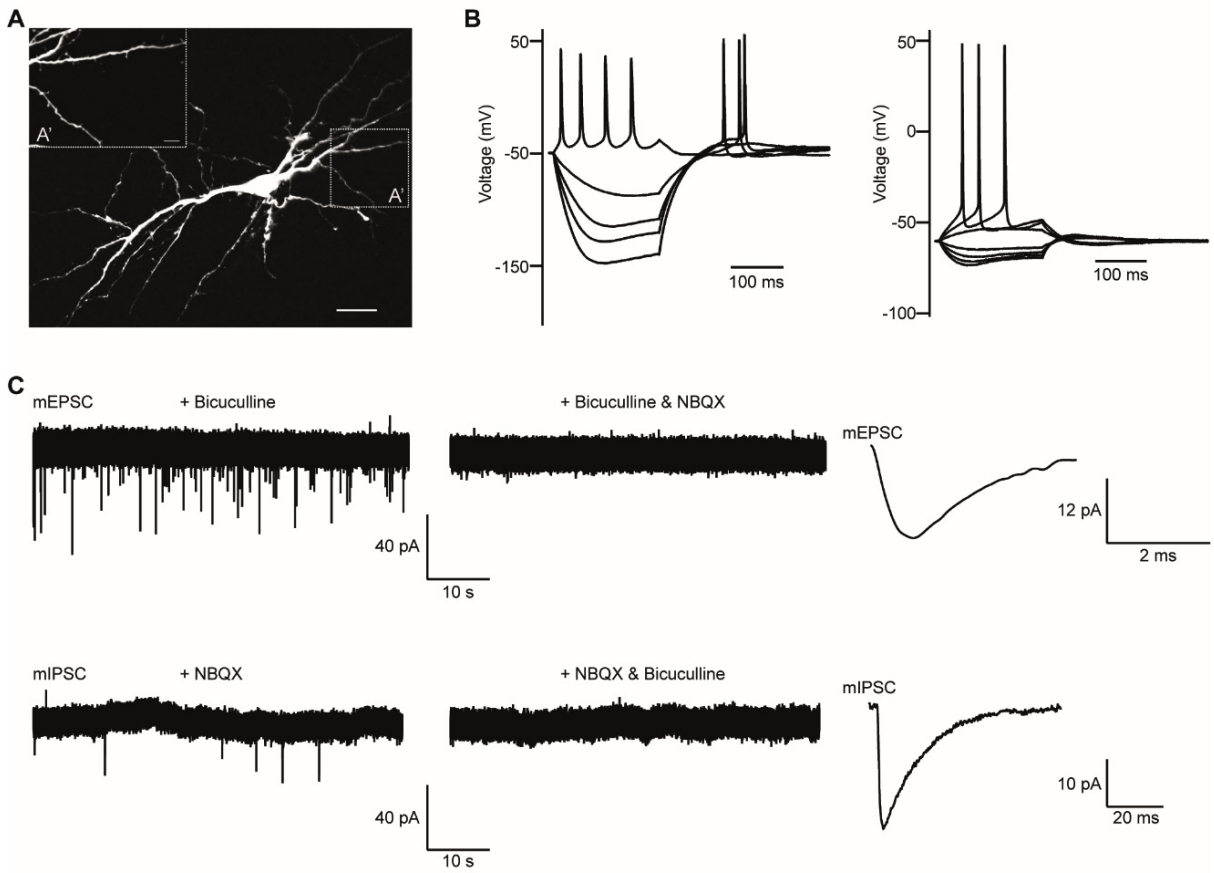

Figure S9. Excitability and functional synaptic connections in control human tissue grafts. (**A**) Representative example of a Lucifer yellow-filled human pyramidal neuron. (**B**) Two examples of current-voltage relationships of two pyramidal shaped GFP-positive human iPSC-derived neurons in human grafts. Potentials are evoked by 200 ms pulses from -80 to +50 pA. (**C**) Top, representative spontaneous miniature excitatory synaptic currents (mEPSC, downward deflections) recorded in voltage-clamp (-70 mV) in the absence (left) and presence of NBQX (5 µM, middle). Mean ensembled mEPSCs from 60 events captured from a single neuron is shown on the right at an expanded time scale. Bottom, spontaneous miniature inhibitory synaptic currents (mIPSC, downward deflections) recorded in symmetrical chloride conditions and in the presence of NBQX (5 µM, left). mIPSC are completely blocked by (+)-bicuculline (middle, 20 µM). Mean ensembled mIPSCs for 40 events from a single neuron is shown on the right at an expanded time scale.

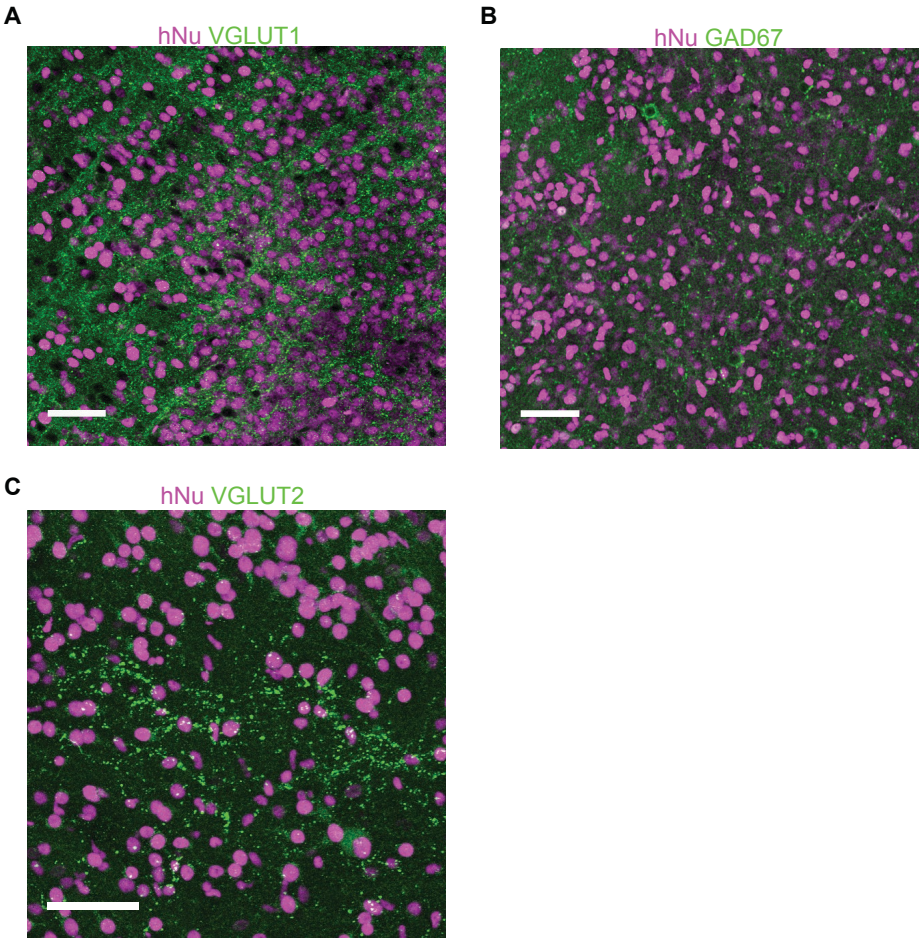

Figure S10. Human grafts contain glutamatergic, GABAergic and thalamocortical terminals. (**A**) Representative example (single plane) of a WT-1 graft stained for Vesicular glutamate transporter 1 (VGLUT1, a marker for excitatory presynaptic terminals; *n* = 2 grafts, at 5 mpt). (**B**) Representative example (single plane) of a WT-1 graft stained for GAD67 (*n* = 3 grafts, at 5 mpt). (**C**) Representative maximum intensity projection (34 planes, 0.5 µm step size) from a WT-2 graft stained for VGLUT2 (a marker for thalamocortical presynaptic terminals) (*n* = 3 grafts at 6 mpt). Scale bars, 50 µm.

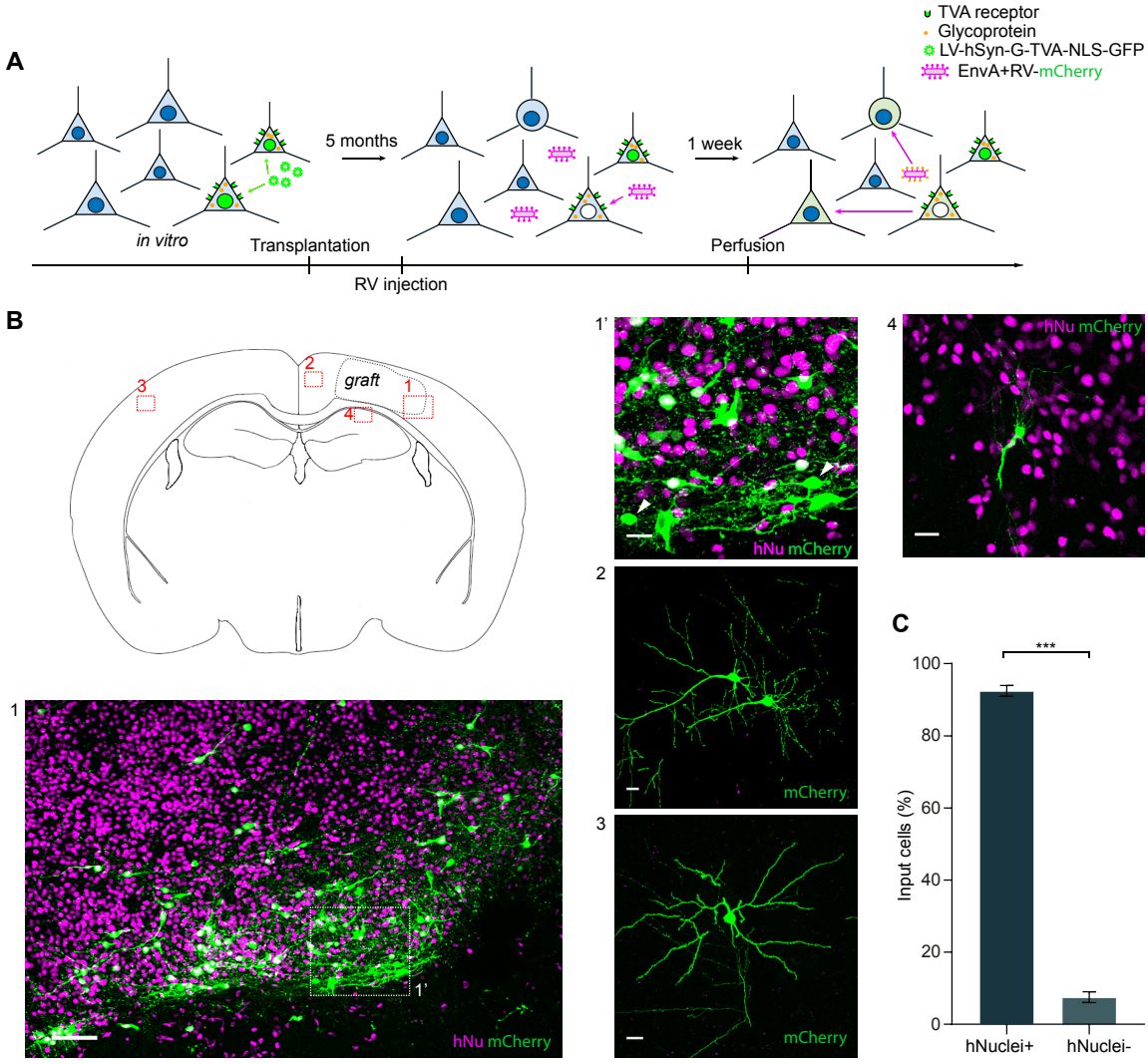

Figure S11. Other human neurons and a small proportion of host neurons are the source of synaptic input. (**A**), Experimental design of retrograde monosynaptic tracing of human neurons with ΔG-rabies virus. (**B**), Location of host input cells in the periphery of the graft (1, 1'), ipsilateral cortex (2), contralateral cortex (3), and in the CA1 region of the ipsilateral hippocampus (4). (**C**), Quantification of human versus host input cells (n = 2 animals, unpaired t-test, ***$P < 0.001$). Scale bars, 100 µm (1) and 20 µm (1', 2, 3, 4).

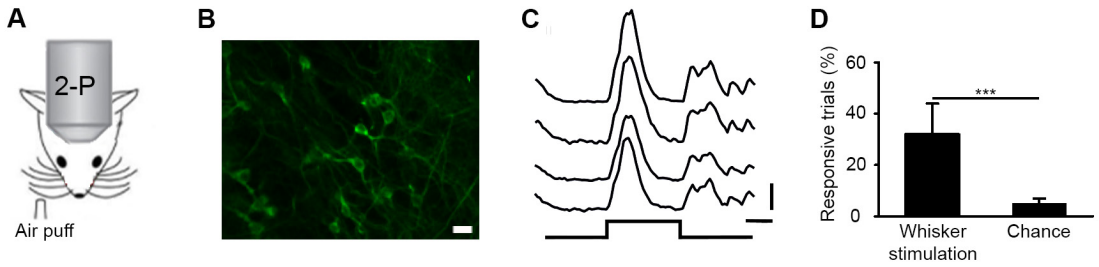

Figure S12. Sensory-evoked activity in human tissue grafts.
(**A**), Cartoon of SCx1 imaging paradigm for whisker stimulation showing mouse under 2P microscope and contralateral whisker stimulation via air puffs. Whisker stimulation was delivered as 8 pulses in 4 trains delivered over 10 seconds. (**B**), Example of imaged cortical regions taken from a WT-1 graft in the Scx1 of an adult mouse. GCaMP6s positive neurons are shown as a maximum intensity projection of activity over a 4 – 5 min period of sensory evoked activity. (**C**), Example of $\%\Delta F/F_0$ calcium traces in response to whisker stimulation for 4 active neurons. Responses are the average of 5 trials. (**D**), Percentage of trials defined as responsive (see methods) during periods with either whisker stimulation (32 ± 12 %, n = 5 regions and 25 trials from one mouse) or with no sensory stimulation (5 ± 2 %, n = 20 regions and 100 trials from 3 mice). Trials without whisker stimulation were used to define the chance levels of measuring a false positive response. The percentage of responsive trials was greater with whisker stimulation (unpaired t-test, $P < 0.001$,). Error bars are mean and s.e.m. Scale bars, 20 µm (**B**), 10 s and 100 % $\Delta F/F_0$ (**C**). The data in this figure is taken from 25 cortical regions across 4 animals.

Marker	Chromo-some	Allele	WT-1	Ts21-1	Ts21 fibro-blast	Ts21-2	WT-2	WT-2’
TPOX	2	1 2						
D3S1358	3	1 2						
FGA	4	1 2	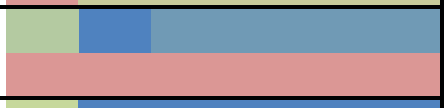					
CSF1PO	5	1 2						
D5S818	5	1 2	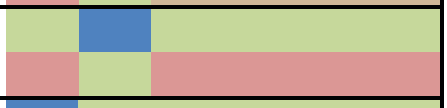					
D7S820	7	1 2						
D8S1179	8	1 2						
TH01	11	1 2						
vWA	12	1 2						
D13S317	13	1 2	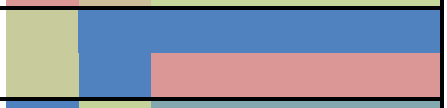					
Penta E	15	1 2						
D16S539	16	1 2	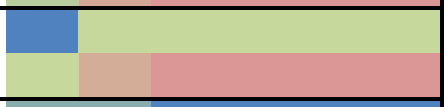					
D18S51	18	1 2						
D21S11	21	1 2 3	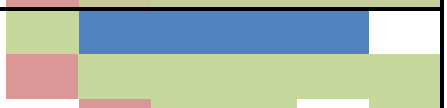					
Penta D	21	1 2 3	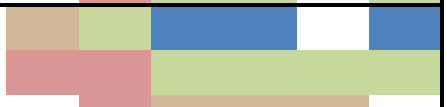					
AMEL	XY	x y	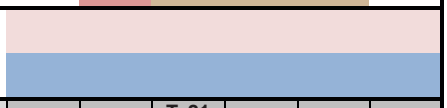					

Figure S13. iPSC-line identity verification. Microsatellite short tandem repeat (STR) assay for WT-1, Ts21-1, WT-2, Ts21-2 iPS cell lines together with the Ts21 fibroblasts, the originating fibroblast lines for the trisomic/revertant disomic pair, and WT-2', a further clone showing spontaneous loss of chromosome 21. Within each locus, varying repeat lengths are discriminated by alternate color. Note that the parental fibroblasts and Ts21-2 are both trisomic for Hsa21 and identical to each other, and that WT-2 and WT-2' are both disomic for different pairs of Hsa21, but otherwise identical to the fibroblasts and Ts21-2.

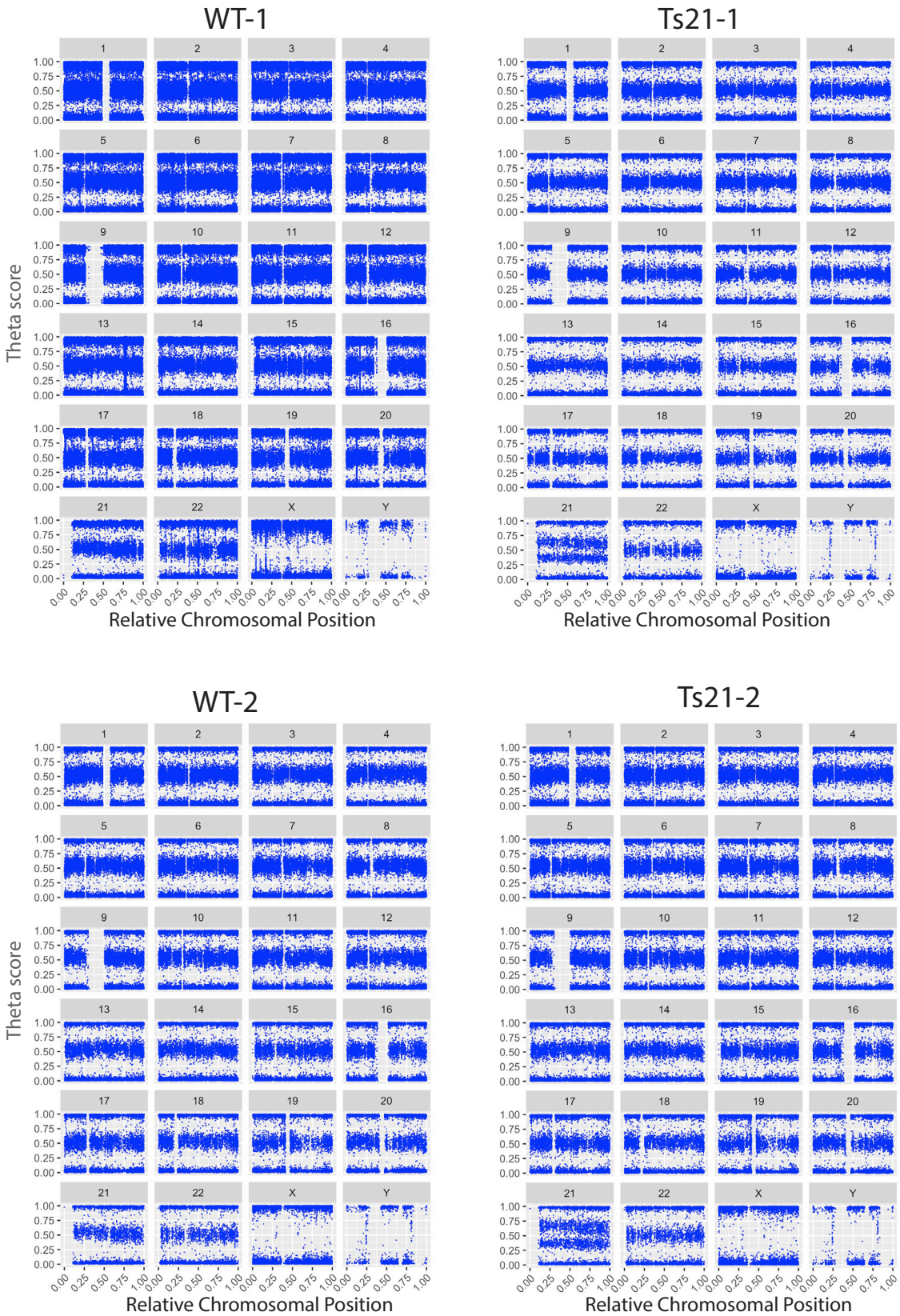

Figure S14. Genome-wide copy number SNP assay. Molecular karyotyping analysis with genome-wide copy number single nucleotide polymorphism (SNP) assay showing

Theta scores (allelic SNP ratio) for individual SNP loci (vertical axis) against normalized distance along chromosome (horizontal axis). Note no major genomic deletions or duplications and expected Ts21 in Ts21-1 and Ts21-2, and euploidy in WT-1 and WT-2.

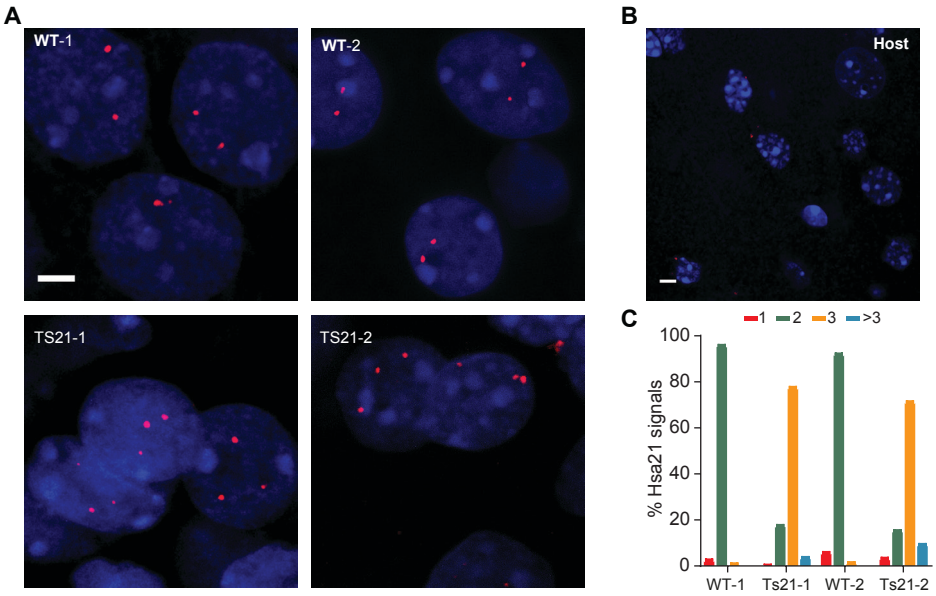

Figure S15. Fluorescent In Situ Hybridization assay (FISH). (**A**) Representative examples of Hsa21-specific FISH signal (red), in each of the four transplanted lines at 5 mpt. Nuclei are counterstained for Dapi (blue). Scale bar, 3 µm. (**B**) Representative example from the host contralateral cortex (negative control). Scale bar, 5 µm. (**C**) Quantification confirming the expected number of XL 21q22 copies in the human tissue grafts from each of the four lines.

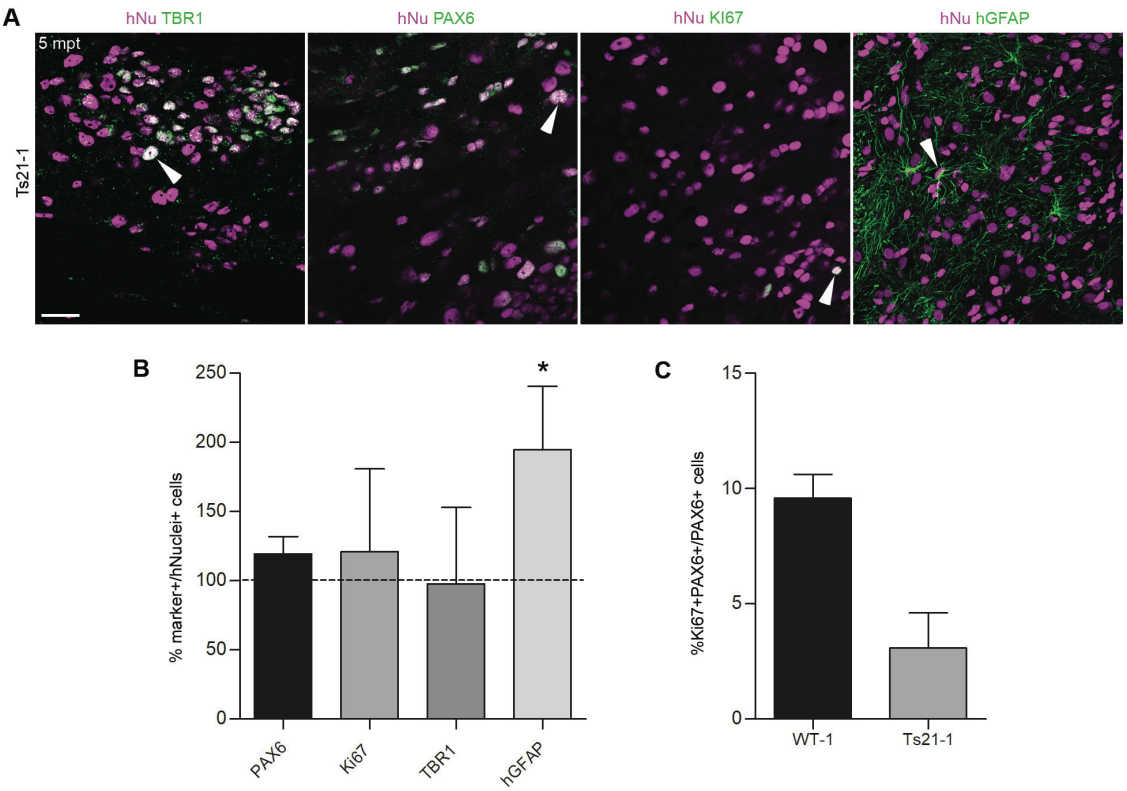

Figure S16. Similar proportion of progenitors, neurons and proliferating cells but increased astroglia in Ts21 human tissue grafts compared to control. (**A**) Representative immunostaining of human Ts21-1 cortical graft for TBR1, PAX6, KI67 and human GFAP at 5 mpt; arrowheads indicate examples positive human cells. Scale bar, 30 µm. (**B**) Relative percentage of Ts21 cell populations *in vivo* ($n = 3$ animals) at 5 mpt (area sampled per cell marker: 1.42 ± 0.76, mean ± SD), normalized to control values (dotted line; area sampled per cell marker: 0.94 ± 0.11, mean ± SD). Unpaired two-tailed *t*-test, $*P < 0.05$. (**C**) Proportion of proliferating PAX6-expressing progenitor cells in WT-1 and Ts21-1 lines at 5 mpt ($n = 2$ mice each line; area sampled: 2.46 ± 0.60 and 1.82 ± 0.18 respectively, mean ± SD). Mann-Whitney U-test, $P = 0.333$.

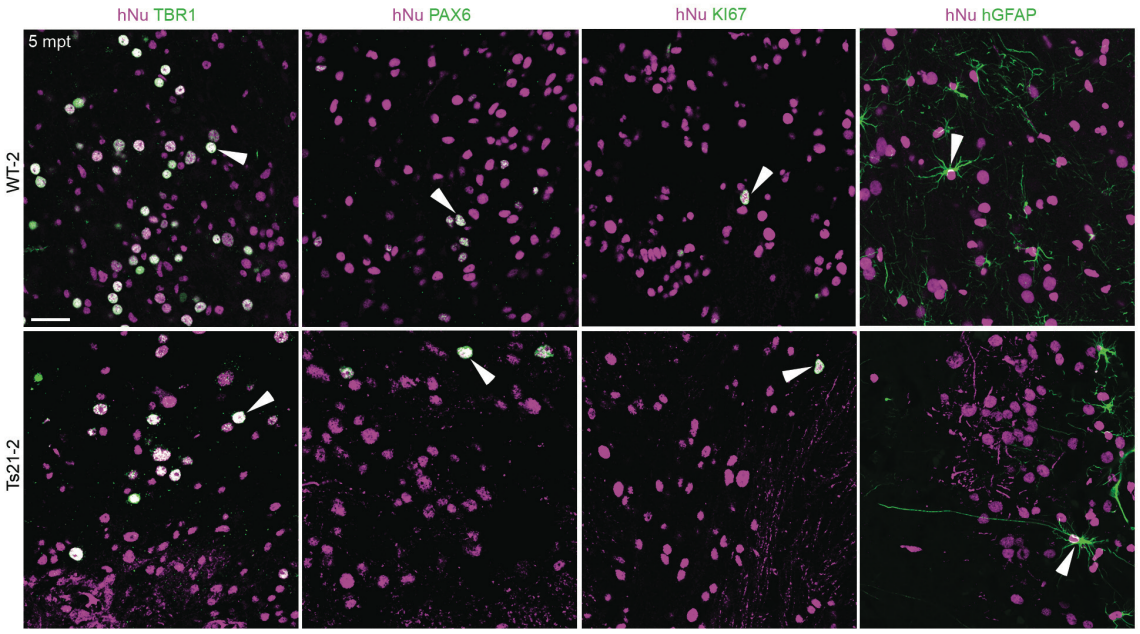

Figure S17. WT-2 and Ts21-2 graft cell identity. Representative immunostaining of human WT-2 and Ts21-2 grafts for TBR1, PAX6, Ki67 and human GFAP at 5 mpt. Arrowheads show examples of positive human cells. Scale bar, 30 µm.

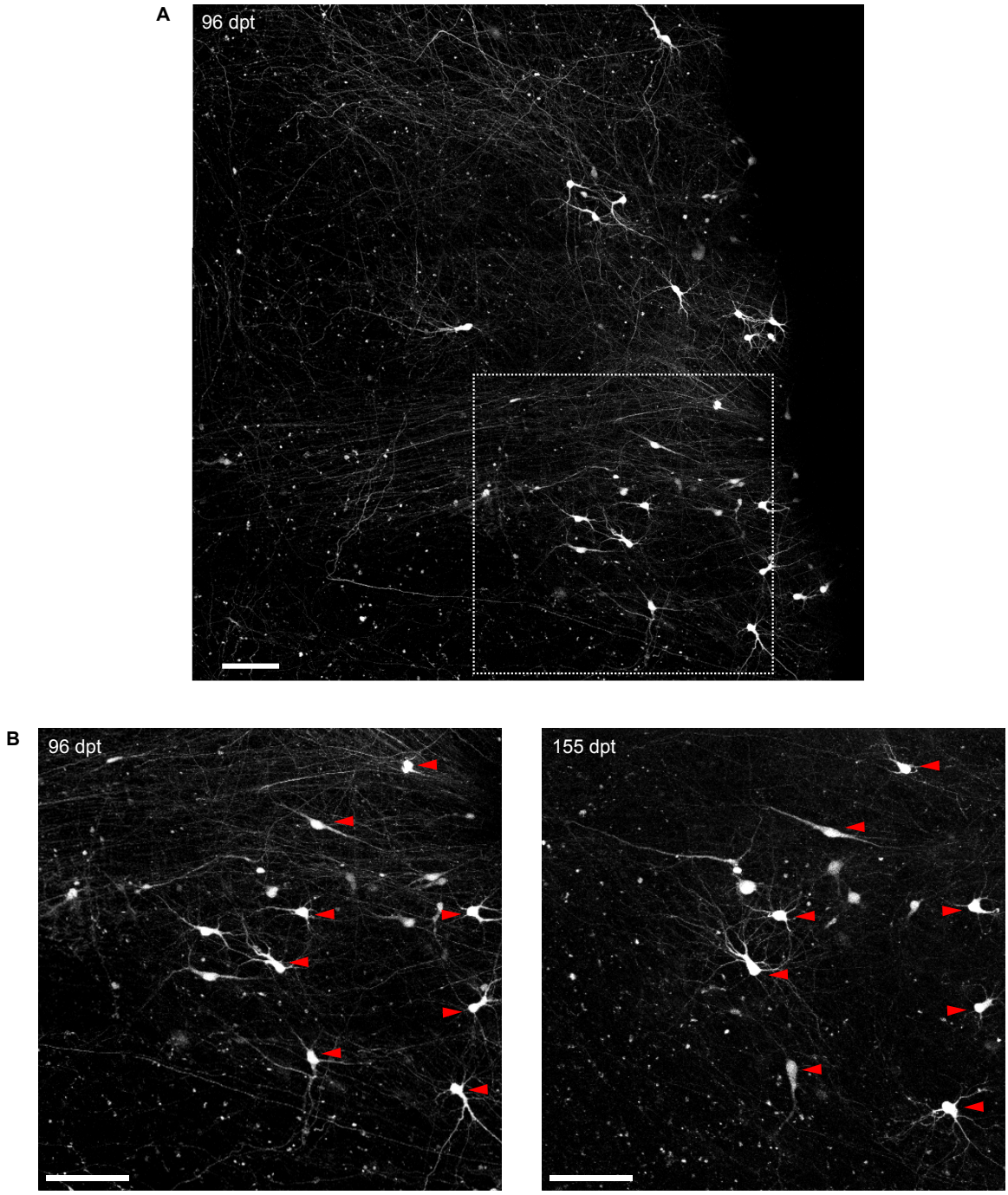

Figure S18. *In vivo* tracking of transplanted Ts21 human neurons over 2 months. (**A**) 2-photon *in vivo* imaging of a Ts21-1 graft at 96 dpt. Scale bar, 100 µm. (**B**) 2-photon *in vivo* imaging of the same graft area (white box in (A)) over the indicated time. Red arrows represent examples of cells with a stable location over a 2-month period. Scale bars, 100 µm.

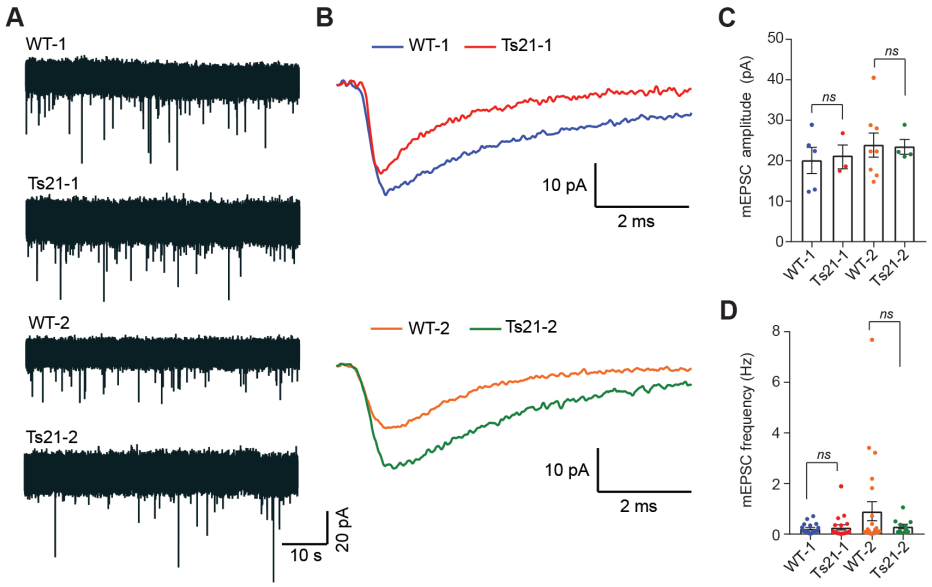

Figure S19. Similar synaptic input in Ts21 neurons compared to control. (**A**) Representative traces of mEPSC recorded in voltage-clamp mode (-70 mV) from WT-1/2 and Ts21-1/2 grafts at 5 mpt. (**B**) Expanded traces of mEPSC shown in A. (**C**, **D**), mEPSC amplitude (WT-1, $n = 5$; Ts21-1, $n = 3$; WT-2, $n = 8$ and Ts21-2, $n = 4$) and frequency (WT-1, $n = 18$; Ts21-1, $n = 19$ cells; WT-2, $n = 23$ and Ts21-2, $n = 11$) in cortical tissue grafts from 3 mice each. Kruskal-Wallis test: amplitude, $P = 0.8395$; frequency, $P = 0.2094$. Each data point represents a cell. *ns*, not significant.

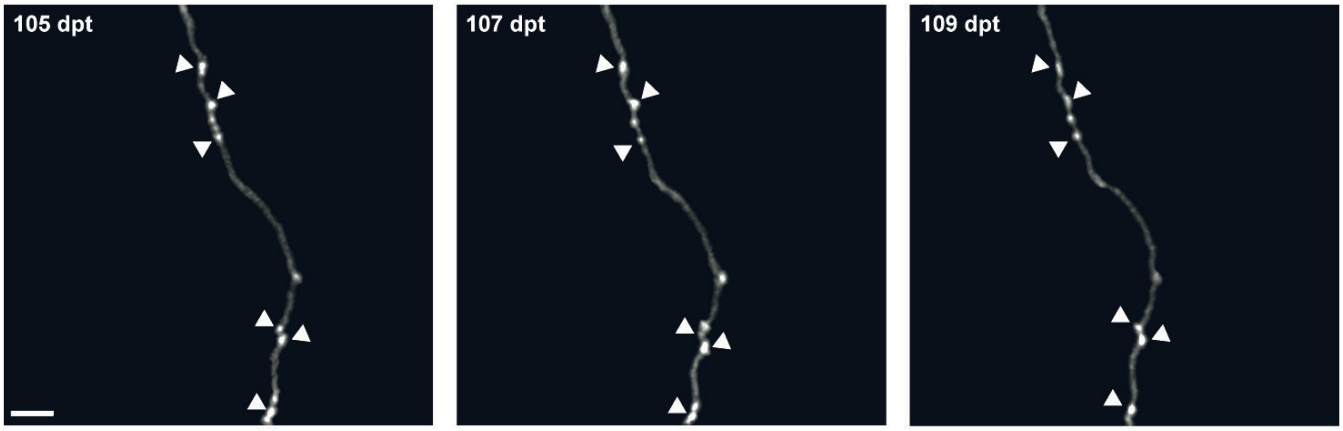

Figure S20. 2-photon *in vivo* imaging of EPB stability on Ts21 neurons. Example of stable EPBs (arrowheads) on Ts21 neurons *in vivo* over the indicated time points. Scale bar, 5 μm.

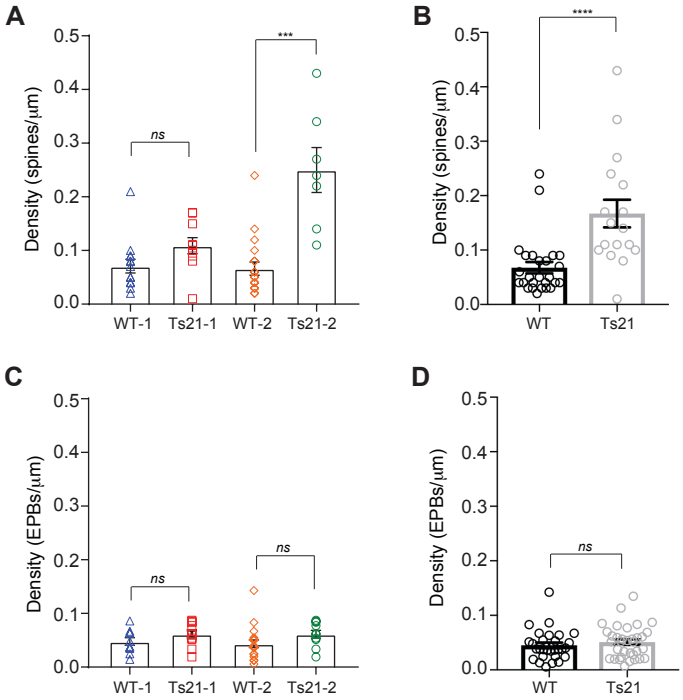

Figure S21. Spine and bouton density in cortical tissue grafts. (**A**) Dendritic spine density at Day 0 in WT-1 (n = 14 cells from 3 animals), Ts21-1 (n = 10 cells from 4 animals), WT-2 (n = 12 cells from 4 animals) and Ts21-2 (n = 7 cells from 2 animals) grafts at 3-4 mpt. Kruskal-Wallis test, ***$P < 0.001$; *ns*, not significant. Each data point represents a cell. (**B**) Dendritic spine density at Day 0 in WT-1/2 (n = 26 cells from 7 animals) and Ts21-1/2 (n = 17 cells from 6 animals) grafts at 3-4 mpt. Mann-Whitney test, ****$P < 0.0001$. Each data point represents a cell. (**C**) EPB density at Day 0 in WT-1 (n = 10 cells from 3 animals), Ts21-1 (n = 10 cells from 3 animals), WT-2 (n = 19 cells from 4 animals) and Ts21-2 (n = 10 cells from 3 animals) in grafts at 3-4 mpt. Kruskal-Wallis test; *ns*, not significant. Each data point represents a cell. (**D**) EPB density at Day 0 in WT-1/2 (n = 29 cells from 7 animals) and Tss21-1/2 (n = 20 cells from 6 animals) in grafts at 3-4 mpt. Mann-Whitney test; *ns*, not significant. Each data point represents a cell.

Table S1.

List of Antibodies.

Antibody	Host Species	Dilution	Reference
Human Nestin (cl. 196908)	Mouse monoclonal	1:1000	R&D Systems, MAB1259
PDFG Receptor α	Rabbit	1:1000	Cell Signaling, 3164
GFP	Chicken	1:300	Novus Biologicals, NB100-1614
Doublecortin	Rabbit	1:400	Cell Signaling, 4604
Ki67	Rabbit	1:1000	Abcam, ab15580
Ki67 (clone B56)	Mouse monoclonal	1:100	BD Biosciences, 550609
Ki67 [OTI5D7]	Rat monoclonal	1:500	Abcam, ab156956
Human Nuclei	Mouse monoclonal	1:200	Millipore, MAB1281
Pax-6	Rabbit	1:300	Biolegend, 901301
NuMA	Rabbit	1:200	Abcam, ab97585
NCAM (ERIC-1)	Mouse monoclonal	1:1000	Santa Cruz Biotechnology, sc-106
Human GFAP	Mouse monoclonal	1:500	Stem123, AB-123-U-050
GFAP	Rabbit	1:1000	DAKO, Z0334
GAD67	Rabbit	1:500	Abcam, ab97739
Iba1	Goat	1:1000	Abcam, ab5076
CD31	Rat	1:200	Biolegend, 102402
TBR1	Rabbit	1:200	Abcam, ab31940
SATB2 [SATBA4B10]	Mouse monoclonal	1:200	Abcam, ab51502
β-actin	Mouse	1:10000	Sigma, A228
APP C-Terminal Fragment	Mouse	1:1000	Biolegend, 802801
TuJ1	Rabbit and Mouse	1:5000	Biolegend, 802001 and 8012021
Synapsin1	Rabbit	1:1000	Abcam, ab8
PSD95	Rabbit	1:1000	Abcam, ab18258
CTIP2 [25B6]	Rat monoclonal	1:300	Abcam, ab18465
OLIG2	Rabbit	1:1000	Millipore, AB9610
VGLUT1	Guinea Pig	1:1000	Millipore, AB5905
VGLUT2	Guinea Pig	1:2000	Synaptic sys., 135-404
DsRed	Rabbit	1:500	Clontech, 632496

Movie S1

Example of WT-1 tissue graft stained for human Neural Cell Adhesion Molecule (NCAM), a human neuron specific antibody, at 5 mpt.

Movie S2

Example of axonal bundles (arrowheads) and vessels (asterisks) in a cortical tissue graft imaged *in vivo* at 3 mpt. Scale bar 50 μm.

Movie S3

Example of axonal layers in a cortical tissue graft imaged *in vivo* at 102 dpt. A montage representation of this 2-photon z-stack is shown in fig. 1F. Scale bar 50 μm.

Movie S4

Example of time series of WT-1 GCaMP6s-expressing human neurons in the adult somatosensory cortex at 5 mpt. Movie was acquired at 3 Hz and is shown at 6 fps. Scale bar, 50 μm.

Movie S5

Example of time series of WT-2 GCaMP6s-expressing human neurons showing stereotypical patterns of population activity *in vivo* at 112 dpt. Movie was acquired at 3 Hz and is shown at 6 fps. A montage representation of this time series is shown in fig. S7I. Scale bar, 50 μm.

Movie S6

Example of time series of Ts21-1 GCaMP6s-expressing human neurons in the adult somatosensory cortex at 5 mpt. Movie was acquired at 3 Hz and is shown at 6 fps. Scale bar, 50 μm.

References

1. W. M. Cowan, J. W. Fawcett, D. D. O'Leary, B. B. Stanfield, Regressive events in neurogenesis. *Science* **225**, 1258-1265 (1984).
2. L. K. Low, H. J. Cheng, Axon pruning: an essential step underlying the developmental plasticity of neuronal connections. *Philos Trans R Soc Lond B Biol Sci* **361**, 1531-1544 (2006).
3. Y. Herault *et al.*, Rodent models in Down syndrome research: impact and future opportunities. *Disease models & mechanisms* **10**, 1165-1186 (2017).
4. A. O'Doherty *et al.*, An aneuploid mouse strain carrying human chromosome 21 with Down syndrome phenotypes. *Science* **309**, 2033-2037 (2005).
5. M. Gupta, A. R. Dhanasekaran, K. J. Gardiner, Mouse models of Down syndrome: gene content and consequences. *Mamm Genome* **27**, 538-555 (2016).
6. I. Espuny-Camacho *et al.*, Hallmarks of Alzheimer's Disease in Stem-Cell-Derived Human Neurons Transplanted into Mouse Brain. *Neuron* **93**, 1066-1081 e1068 (2017).
7. J. van den Ameele, L. Tiberi, P. Vanderhaeghen, I. Espuny-Camacho, Thinking out of the dish: what to learn about cortical development using pluripotent stem cells. *Trends Neurosci* **37**, 334-342 (2014).
8. Y. Shi, P. Kirwan, J. Smith, H. P. Robinson, F. J. Livesey, Human cerebral cortex development from pluripotent stem cells to functional excitatory synapses. *Nat Neurosci* **15**, 477-486, S471 (2012).
9. M. A. Lancaster *et al.*, Cerebral organoids model human brain development and microcephaly. *Nature* **501**, 373-379 (2013).
10. P. Carmeliet, M. Tessier-Lavigne, Common mechanisms of nerve and blood vessel wiring. *Nature* **436**, 193-200 (2005).
11. L. H. Thompson, A. Bjorklund, Reconstruction of brain circuitry by neural transplants generated from pluripotent stem cells. *Neurobiol Dis* **79**, 28-40 (2015).
12. J. S. Barbosa *et al.*, Neurodevelopment. Live imaging of adult neural stem cell behavior in the intact and injured zebrafish brain. *Science* **348**, 789-793 (2015).
13. Y. Shi, P. Kirwan, F. J. Livesey, Directed differentiation of human pluripotent stem cells to cerebral cortex neurons and neural networks. *Nat Protoc* **7**, 1836-1846 (2012).
14. M. E. Emborg *et al.*, Induced pluripotent stem cell-derived neural cells survive and mature in the nonhuman primate brain. *Cell reports* **3**, 646-650 (2013).
15. X. Qian *et al.*, Brain-Region-Specific Organoids Using Mini-bioreactors for Modeling ZIKV Exposure. *Cell* **165**, 1238-1254 (2016).
16. A. Hoerder-Suabedissen, Z. Molnar, Development, evolution and pathology of neocortical subplate neurons. *Nat Rev Neurosci* **16**, 133-146 (2015).
17. T. Saito *et al.*, Neocortical layer formation of human developing brains and lissencephalies: consideration of layer-specific marker expression. *Cereb Cortex* **21**, 588-596 (2011).
18. N. Palomero-Gallagher, K. Zilles, Cortical layers: Cyto-, myelo-, receptor- and synaptic architecture in human cortical areas. *Neuroimage*, (2017).
19. I. M. Zakiewicz, J. G. Bjaalie, T. B. Leergaard, Brain-wide map of efferent projections from rat barrel cortex. *Front Neuroinform* **8**, 5 (2014).

20. I. Espuny-Camacho *et al.*, Pyramidal neurons derived from human pluripotent stem cells integrate efficiently into mouse brain circuits in vivo. *Neuron* **77**, 440-456 (2013).
21. L. Luo, D. D. O'Leary, Axon retraction and degeneration in development and disease. *Annu Rev Neurosci* **28**, 127-156 (2005).
22. A. Nikolaev, T. McLaughlin, D. D. O'Leary, M. Tessier-Lavigne, APP binds DR6 to trigger axon pruning and neuron death via distinct caspases. *Nature* **457**, 981-989 (2009).
23. C. Portera-Cailliau, R. M. Weimer, V. De Paola, P. Caroni, K. Svoboda, Diverse modes of axon elaboration in the developing neocortex. *PLoS Biol* **3**, e272 (2005).
24. V. De Paola *et al.*, Cell type-specific structural plasticity of axonal branches and boutons in the adult neocortex. *Neuron* **49**, 861-875 (2006).
25. V. De Paola, S. Arber, P. Caroni, AMPA receptors regulate dynamic equilibrium of presynaptic terminals in mature hippocampal networks. *Nat Neurosci* **6**, 491-500. (2003).
26. P. Caroni, F. Donato, D. Muller, Structural plasticity upon learning: regulation and functions. *Nat Rev Neurosci* **13**, 478-490 (2012).
27. T. L. Petit, J. C. LeBoutillier, D. P. Alfano, L. E. Becker, Synaptic development in the human fetus: a morphometric analysis of normal and Down's syndrome neocortex. *Exp Neurol* **83**, 13-23 (1984).
28. P. R. Huttenlocher, A. S. Dabholkar, Regional differences in synaptogenesis in human cerebral cortex. *J Comp Neurol* **387**, 167-178 (1997).
29. M. E. Molliver, I. Kostovic, H. van der Loos, The development of synapses in cerebral cortex of the human fetus. *Brain Res* **50**, 403-407 (1973).
30. A. Holtmaat *et al.*, Long-term, high-resolution imaging in the mouse neocortex through a chronic cranial window. *Nat Protoc* **4**, 1128-1144 (2009).
31. O. Garaschuk, J. Linn, J. Eilers, A. Konnerth, Large-scale oscillatory calcium waves in the immature cortex. *Nat Neurosci* **3**, 452-459 (2000).
32. R. Khazipov, H. J. Luhmann, Early patterns of electrical activity in the developing cerebral cortex of humans and rodents. *Trends Neurosci* **29**, 414-418 (2006).
33. P. Kirwan *et al.*, Development and function of human cerebral cortex neural networks from pluripotent stem cells in vitro. *Development* **142**, 3178-3187 (2015).
34. G. Quadrato *et al.*, Cell diversity and network dynamics in photosensitive human brain organoids. *Nature* **545**, 48-53 (2017).
35. T. W. Chen *et al.*, Ultrasensitive fluorescent proteins for imaging neuronal activity. *Nature* **499**, 295-300 (2013).
36. S. Vanhatalo *et al.*, DC-EEG discloses prominent, very slow activity patterns during sleep in preterm infants. *Clin Neurophysiol* **113**, 1822-1825 (2002).
37. P. J. Uhlhaas, F. Roux, E. Rodriguez, A. Rotarska-Jagiela, W. Singer, Neural synchrony and the development of cortical networks. *Trends Cogn Sci* **14**, 72-80 (2010).
38. A. A. Mansour *et al.*, An in vivo model of functional and vascularized human brain organoids. *Nat Biotechnol*, (2018).
39. C. Chen *et al.*, Role of astroglia in Down's syndrome revealed by patient-derived human-induced pluripotent stem cells. *Nature communications* **5**, 4430 (2014).

40. G. A. Maclean *et al.*, Altered hematopoiesis in trisomy 21 as revealed through in vitro differentiation of isogenic human pluripotent cells. *Proc Natl Acad Sci U S A* **109**, 17567-17572 (2012).
41. J. P. Weick *et al.*, Deficits in human trisomy 21 iPSCs and neurons. *Proc Natl Acad Sci U S A* **110**, 9962-9967 (2013).
42. K. Plona, T. Kim, K. Halloran, A. Wynshaw-Boris, Chromosome therapy: Potential strategies for the correction of severe chromosome aberrations. *Am J Med Genet C Semin Med Genet* **172**, 422-430 (2016).
43. E. Dossi, F. Vasile, N. Rouach, Human astrocytes in the diseased brain. *Brain research bulletin* **136**, 139-156 (2018).
44. K. Mollgard, J. J. Lundberg, B. K. Beebe, A. Bjorklund, U. Stenevi, The intracerebrally cultured 'microbrain': a new tool in developmental neurobiology. *Neurosci Lett* **8**, 295-301 (1978).
45. S. Falkner *et al.*, Transplanted embryonic neurons integrate into adult neocortical circuits. *Nature* **539**, 248-253 (2016).
46. J. A. Korecka, S. Levy, O. Isacson, In vivo modeling of neuronal function, axonal impairment and connectivity in neurodegenerative and neuropsychiatric disorders using induced pluripotent stem cells. *Mol Cell Neurosci* **73**, 3-12 (2016).
47. D. Tornero *et al.*, Synaptic inputs from stroke-injured brain to grafted human stem cell-derived neurons activated by sensory stimuli. *Brain* **140**, 692-706 (2017).
48. P. Lu *et al.*, Long-distance growth and connectivity of neural stem cells after severe spinal cord injury. *Cell* **150**, 1264-1273 (2012).
49. V. Tabar *et al.*, Migration and differentiation of neural precursors derived from human embryonic stem cells in the rat brain. *Nat Biotechnol* **23**, 601-606 (2005).
50. M. Wernig *et al.*, Neurons derived from reprogrammed fibroblasts functionally integrate into the fetal brain and improve symptoms of rats with Parkinson's disease. *Proc Natl Acad Sci U S A* **105**, 5856-5861 (2008).
51. M. Mandai *et al.*, Autologous Induced Stem-Cell-Derived Retinal Cells for Macular Degeneration. *N Engl J Med* **376**, 1038-1046 (2017).
52. H. Q. Huo *et al.*, Modeling Down Syndrome with Patient iPSCs Reveals Cellular and Migration Deficits of GABAergic Neurons. *Stem Cell Reports* **10**, 1251-1266 (2018).
53. M. A. Israel *et al.*, Probing sporadic and familial Alzheimer's disease using induced pluripotent stem cells. *Nature* **482**, 216-220 (2012).
54. I. H. Park *et al.*, Disease-specific induced pluripotent stem cells. *Cell* **134**, 877-886 (2008).
55. A. J. Peters, S. X. Chen, T. Komiyama, Emergence of reproducible spatiotemporal activity during motor learning. *Nature* **510**, 263-267 (2014).
56. L. Regeur, B. Pakkenberg, Optimizing sampling designs for volume measurements of components of human brain using a stereological method. *J Microsc* **155**, 113-121 (1989).
57. F. W. Grillo *et al.*, Increased axonal bouton dynamics in the aging mouse cortex. *Proc Natl Acad Sci U S A* **110**, E1514-1523 (2013).
58. A. Dubbs, J. Guevara, R. Yuste, moco: Fast Motion Correction for Calcium Imaging. *Front Neuroinform* **10**, 6 (2016).

59. S. J. Barnes *et al.*, Subnetwork-Specific Homeostatic Plasticity in Mouse Visual Cortex In Vivo. *Neuron* **86**, 1290-1303 (2015).
60. R. P. Sammons, C. Clopath, S. J. Barnes, Size-Dependent Axonal Bouton Dynamics following Visual Deprivation In Vivo. *Cell reports* **22**, 576-584 (2018).